Kinetic modelling of Cr_2O_3 growth on a Ni-30Cr alloy in silicate melts

E. Schmucker, V. Szczepan, L. Martinelli, C. Petitjean, P.J. Panteix, S. Ben Lagha, M. Vilasi

Version of Record: https://www.sciencedirect.com/science/article/pii/S0010938X20312919
Manuscript_94da1889b785700b17e0b7e1e609d364

Kinetic modelling of Cr_2O_3 growth on a Ni-30Cr alloy in silicate melts

E. Schmucker[a,c*], V. Szczepan[a], L. Martinelli[b], C. Petitjean[a], P.J. Panteix[a], S. Ben Lagha[c], M. Vilasi[a]

[a] *Université de Lorraine, CNRS, IJL, F-54011 Nancy, France.*

[b] *CEA, Université Paris-Saclay, Den-Service de la Corrosion et du Comportement des Matériaux dans leur Environnement (SCCME), F-91191, Gif-sur-Yvette, FRANCE.*

[c] *Orano, 125 avenue de Paris, F-92320, Châtillon, FRANCE*

*corresponding author
e-mail: eric.schmucker@outlook.fr

Abstract

Corrosion tests of Ni-30Cr alloy were performed in three simplified soda-silicate and borosilicate melts in order to follow the evolution of the protective chromia layer. A complete identification of the corrosion mechanisms enables the establishment of a kinetic model based on the oxide formation and dissolution rates. The dissolution kinetics is strongly dependent on the chromium solubility limit and diffusivity, which are related to the basicity and viscosity of the melts. This new modelling of the oxide growth is in good agreement with the experimental results.

Keywords: A. Alloy ; A. Glass ; B. Modelling studies; B. SEM; C. High temperature corrosion ; B. Kinetic parameters

1. Introduction

The high chromium content of nickel-based chromia-forming alloys confers them a higher resistance against corrosion by glass melts at high temperature. Indeed, the development of a protecting Cr_2O_3 layer, with low solubility in the melts [1-7], limits the interactions between the metal and the corroding medium [8-11]. The lifetime of the alloy thus depends directly on the durability of the oxide layer, which is a permanent competition

between its simultaneous growth and recession. It has been shown that the formation of the protecting Cr_2O_3 layer on Ni-30Cr alloys is possible due to (i) a sufficient chromium concentration at the alloy/oxide interface and (ii) a sufficient chromium gradient in the alloy ensuring chromium diffusion from the core towards the surface [12]. On the contrary, the oxide dissolution is directly linked to the Cr physicochemistry in the melts (*i.e.* its solubility and its diffusion coefficient) which depends on intrinsic properties of the melt (i.e. its basicity and its viscosity) [13].

Indeed, properties of the melt may influence the behaviour of dissolved elements through their oxidation state, their complexation and their diffusion. For example, the dissolution of Cr_2O_3 into Cr^{III} species is the result of an acido-basic reaction due to the acidic properties of the melt. Three species of chromium can be encountered in molten silicates: Cr^{II}, Cr^{III} and Cr^{VI} [3-5]. Consequently, according to the redox conditions, the dissolved Cr^{III} species can be oxidised to Cr^{VI} or reduced to Cr^{II}. Previous studies have dealt with the solubility of Cr_2O_3 in simplified binary (Na_2O-SiO_2) and ternary (Na_2O-CaO-SiO_2) systems, focusing on the influence of temperature, oxygen fugacity and basicity of the melt [3-6]. A minimum of solubility has been measured in intermediate oxygen fugacity, corresponding to the stability domain of Cr^{III}. The speciation to Cr^{VI} or Cr^{II} leads to an increase of the solubility. Cr^{VI} forms chromates with four free oxygen O^{2-} (tetrahedral coordination) and is thus stabilised in basic melts [14,15]. Cr^{II} is in octahedral coordination with non-bridging oxygen of the network [15,16]. It can thus be considered as a network modifier, leading to its higher stability in polymerised networks (*i.e.* acidic melts). The diffusion of Cr species has also been measured by electrochemical methods in different types of melts [13,17-22]. In all cases, the diffusion of Cr^{III} is favoured in low viscosity melts, as the diffusion coefficient of Cr^{III} increases about one order of magnitude when the melt viscosity is two orders of magnitude lower. Cr^{VI} has a diffusion coefficient much lower than Cr^{III} (two orders of magnitude), which can be attributed to the formation of chromates with much higher valence state of Cr^{VI}.

In a previous work, the chromium solubility limit in atmospheres ranging from oxygen fugacity = 10^{-13} to 0.2 atm, as well as the diffusion coefficients of Cr^{II}, Cr^{III} and Cr^{VI} species have been determined experimentally at 1150°C in three simplified soda silicate and soda-borosilicates melts [13]. The data have been correlated with the corrosion behaviour of a preoxidised model Ni-30Cr alloy immersed in the same melts. However, the conclusions of this previous work only constitute a qualitative approach of the corrosion behaviour of chromia-forming alloys in contact with molten silicates, as it gives a binary insight on the

stability or the instability of the layer depending on the basicity and the viscosity of the melt. Gheno *et al.* recently published the following analytical solution for a parabolic oxide growth in molten silicates [23,24]:

$$x^2 = 2gt \quad \text{Equation 1}$$

$$g = {k_\mathrm{d}}^2 + k_\mathrm{p} - k_\mathrm{d}\sqrt{{k_\mathrm{d}}^2 + k_\mathrm{p}} \quad \text{Equation 2}$$

With :

$$k_\mathrm{d} = \frac{M_\mathrm{MO}}{\rho_\mathrm{MO}} S_M \sqrt{\frac{D_\mathrm{M}}{\pi}} \quad \text{Equation 3}$$

M_MO and ρ_MO are the molar weight and the density of the oxide respectively. S_M and D_M are the cation solubility limit and diffusion coefficient in the melt. g is the parabolic rate constant for the oxide growth in the melt, k_p and k_d are the rate constants for the oxide formation and dissolution respectively. However this equation is only valid when no initial oxide is present at the beginning of immersion. For Cr-rich alloys, a preoxidation treatment is essential to ensure a protection against corrosion in molten silicates [25,26]. Indeed, non-preoxidised alloys can endure severe corrosion and penetration of the melt [26-28]. Therefore, the aim of this article is to identify the mechanisms ruling the corrosion and to establish a new kinetic model of the time evolution of the thickness of the oxide layer of preoxidised Cr-rich alloys.

2. Materials and methods

2.1. Alloy and glass melts compositions

The synthesis, characterisation and properties of the Ni-30Cr alloy used in this study have been stated in previous papers [12,29]. Its composition is 30.5 ± 1.2 wt.% Cr. The three glass compositions used for the immersion tests are: Na_2O-3SiO_2 (N3S), 0.75Na_2O-B_2O_3-2.75SiO_2 (0.75NB2.75S) and 2.3Na_2O-B_2O_3-5SiO_2 (2.3NB5S). Their synthesis and properties

are given in reference [13]. The same glass batches as in ref [13] have been used for this study. These compositions were selected in order to compare the effects of both basicity and viscosity of the melts on the corrosion behaviour of the alloy. The melts properties are recalled in Table 1.

2.2. Immersion tests of Ni-30Cr in silicate melts

The following procedure has been applied to carry out the immersion tests: Ni-30Cr samples with a rod shape (diameter = 5 mm; height = 25 mm) were ground with a P1200 SiC paper, then mounted in refractory mullite tubes and sealed with an alumina cement. Prior to the immersion, Ni-30Cr were submitted to a preoxidation treatment in air during 2 h at 1150°C, 1 cm above the glass batch – about 800 g of glass melt in a Pt-10%Rh crucible – in order to form an initial Cr_2O_3 layer at the surface of the alloy. This preoxidation treatment is necessary to initiate the formation of Cr_2O_3 because of the stability of Cr^{II} species in glass melts that can hinder the oxidation of chromium to the valence +3. The alloy is therefore directly in its passive state when immersed [13,26]. In these conditions (2h at 1150 °C), the thickness of the Cr_2O_3 preoxidation layer is in the range from 2.6 to 4.4 µm (Fig. 1) [13]. Immersions are then performed in the glass melts at 1150°C for several durations ranging from 30 min up to 51 h depending on the glass melt. One single sample was used for each duration. At the end of immersion, samples were cooled in air and embedded in an epoxy resin before cross-sectioning and polishing for SEM observations and EPMA analyses.

2.3. Characterisation

After embedding in epoxy resin, cutting and mirror polishing of the immersed samples, SEM observations of the cross-sections of the samples were performed with a JEOL J7600F apparatus in BSE contrast mode with an acceleration voltage of 7 kV. The average thicknesses of the Cr_2O_3 layer after immersions have been assessed through 15-20 measurements on SEM micrographs on the whole periphery of the sample. Error bars are represented by the standard deviation of these measurements.

Chromium depletion profiles in the alloy have been measured by SEM coupled with EDX analyses with an acceleration voltage of 20 kV. Pure chromium and nickel have been used as standards for quantification.

Chromium diffusion profiles in the glass melts have been determined with a CAMECA SX 100 Electron Probe MicroAnalyser (EPMA) with a 20 µm large beam spot in order to minimise the sodium migration under the electron beam [30]. Detailed analysis conditions for these glass phases are given in a previous paper [13].

3. Experimental results

3.1. Features of the alloy/oxide/melt interface and oxide thickness evolution

Corrosion experiments with preoxidised Ni-30Cr samples were performed at 1150°C for durations up to 51 h in the N3S melt, 25 h in the 0.75NB2.75S melt and 2 h in the 2.3NB5S melt. A depassivation phenomenon leading to the dissolution of the oxide layer rapidly occurred on the samples immersed in 2.3NB5S [13]. Then, only short immersion runs, up to 2 h, were carried out in this melt. The present study focuses on the corrosion behaviour of Ni-30Cr in the passive state, as long as the oxide layer is present. The characteristic features of the interfaces between the alloy and melts are shown in Fig. 2a, b and c. A compact and covering Cr_2O_3 layer has been evidenced by EDX measurement at the alloy/glass interface after immersion in each melt. Porosities are visible within the alloy beneath the oxide scale. These porosities arise after vacancies condensation due to Kirkendall effect or vacancies injection by the oxidation process [12,31].

The evolutions of the measured thicknesses of the Cr_2O_3 layer grown on the preoxidised Ni-30Cr alloy after immersions in the different glass melts at 1150°C are represented on Fig. 3a, b and c. In the N3S and 0.75NB2.75S melts, the oxide thickness does not vary much within the first 1-4 hours, then a slow growth of few micrometers of the oxide layer occurred (Fig. 3a and b), while the Cr_2O_3 did not grow with a thickness remaining constant at about only 3 µm during 2 h of immersion in the 2.3NB5S melt (Fig. 3c).

3.2. Chromium depletion in the alloy

The formation of the Cr_2O_3 layer is the consequence of the reaction between metallic chromium from the alloy and the dioxygen O_2 dissolved in the silicate melts [32-34]. The establishment of the oxide layer induces a consumption of chromium from the alloy, resulting in a depletion profile underneath the oxide layer. Depletion profiles in the Ni-30Cr alloys after different immersion durations in the melts are presented in Fig. 4a, b and c. Both the depletion depth and the chromium content at the oxide/alloy interface increase with time. The latter tends to stabilise at values superior to 20 wt.%. These observations are consistent with the results obtained for the oxidation of Ni-30Cr alloy at 1150°C in gaseous atmospheres with PO_2 ranging from 10^{-12} up to 10^{-3} atm [12].

3.3. Chromium diffusion in the melts

In order to identify the dissolution mechanism of the Cr_2O_3 layer in the silicate melts, diffusion profiles of chromium in the glasses have been measured by EPMA from the oxide/glass interface. Chromium diffusion profiles in each glass melt are presented for several immersion durations in Fig. 5. First of all, it appears that the chromium content at the oxide/glass interface does not vary much with the immersion duration for a given melt. In the N3S and 2.3NB5S melts, which have the same optical basicity (Table 1), this chromium content is close to 0.5 at.%. In the 0.75NB2.75S melt, which is more acidic, the chromium content at the oxide/glass interface is about 0.3 at.% after 30 minutes. The lower interfacial chromium content in the 0.75NB2.75S melt after 8 hours might be explained by chemical modification of the glass by alumina dissolution from the mullite tube or by volatilisation of borate entities for long high temperature treatment [35,36]. Indeed the 0.75NB2.75S melt was the most subjected to a chemical modification of its composition during heat treatment [37]. Therefore, the basicity of the melt is likely to have an influence on the dissolution process of the Cr_2O_3 layer. Besides, the diffusion lengths of chromium after 30 min of immersion is greater in the borosilicate melts which have the lowest viscosities and is lower in the N3S melt which has the highest viscosity amongst the studied melts. As expected, this diffusion length increases with time for each melt. Furthermore, a visual observation of the samples after removal from the glass batch showed a greenish-yellowish colouring which is characteristic of the presence of Cr^{III}/Cr^{VI} in the glass [15].

4. Corrosion mechanisms of Ni-30Cr in silicate melts

In order to propose a suitable modelling of the corrosion kinetics, the limiting steps of the Cr_2O_3 layer formation and dissolution kinetics have to be clearly identified. The aim of the following section is to elucidate these mechanisms on the basis of the experimental results presented before.

4.1. Formation of the Cr_2O_3 layer

The growth of the Cr_2O_3 layer is maintained by the oxidation of chromium into Cr^{III} species by the dissolved oxygen from the melt. The formation kinetics of the Cr_2O_3 layer can be limited by (i) the supply of oxygen from the melt, (ii) the supply of chromium from the alloy or (iii) the diffusion of chromium or oxygen atoms through the oxide layer.

As long as the homogeneous Cr_2O_3 scale is present, the alloy is in the passive state and its corrosion potential has a high value comprised between approximately -900 mV and -50 mV (*vs.* Yttria-Stabilised Zirconia electrode) at 1150 °C [13]. Such values indicate that the oxidising species is the dissolved oxygen from the melt [33,34]. In the case of an insufficient supply of oxygen, the oxidant becomes Si^{IV} entities from the melt and the corrosion potential decreases to values inferior to -1 V with the oxidation of Cr^0 into Cr^{II} instead of Cr^{III}. In the light of this knowledge, since the samples studied here stays in the passive state, the hypothesis of a limitation of the oxide formation kinetics by the lack of oxygen supply can be excluded.

Furthermore, Fig. 4 shows that the chromium content at the alloy/oxide interface stabilises at value between 20 and 24 wt.% in each melt. These values are similar to the ones encountered in gaseous oxidation of the Ni-30Cr alloy at 1150°C and are sufficient to provide enough chromium for the continuous formation of the Cr_2O_3 layer in Ni-30Cr alloy [12,38]. Consequently, the formation rate of the chromium oxide must be limited by the diffusion of ionic species through the layer. Therefore, this formation kinetics will be assimilated to the oxidation kinetics in oxygen atmosphere, which is governed by ionic diffusion and independent on the PO_2 between 10^{-13} and 10^{-2} atm O_2 at 1150°C: the parabolic constant rate, k_p, associated to the formation rate is 5.0×10^{-12} cm^2 s^{-1} [29].

4.2. Dissolution of the Cr_2O_3 layer

As for the formation of Cr_2O_3, different steps can be limiting for the dissolution rate of Cr_2O_3 in the melt. It can be limited either by the interfacial dissolution reaction or by the diffusion of chromium species in the melt.

The diffusion profiles of chromium in the melts in Fig. 5 show that the chromium content at the oxide/melt interface is constant over time and close to the Cr^{III} solubility limit for a given melt. This statement is less obvious for the 0.75NB2.75S melt but the volatilisation of borate entities can occur and the inherent chemical modification of the melt, affecting the solubility of chromium, should be kept in mind. Moreover, about 1 wt.% Al_2O_3 was measured at the oxide/glass interface after 30 min in the 0.75NB2.75S melt and about 6-7 wt.% after 8 h. Thus the dissolution of alumina from the refractory sample holder also contributes to this modification. The addition of alumina in the glass melt may diminish the solubility of chromium in the same manner as it has been evidenced for tin [39]. In the N3S melt, the alumina content at the interface is only about 0.1 wt.% after 9 h and 0.5 wt.% after 51 h, which is less likely to have an influence on the solubility of chromium. No measurements of alumina contents in the 2.3NB5S have been performed. Furthermore, measurements are performed with a 20 µm beam spot and the oxide layer must not be analysed by the beam. These precautions lower the accuracy of the interfacial chromium content measurements, especially as these contents are very low. To conclude, the interfacial chromium contents can be considered stable over time, so the dissolution kinetics is not limited by the interfacial dissolution reaction but by the diffusion of chromium through the melt.

The presence of Cr^{II} species in the melt is impossible since it would imply a redox potential of the glass insufficient to form a Cr_2O_3 layer on the alloy. Therefore, the remaining question is to determine whether it is Cr^{III} or Cr^{VI} species that are limiting the diffusion through the melt. On one hand, the interfacial chromium content is close to the solubility limit of Cr^{III} in each melt: 0.45 at.% in N3S and 2.3NB5S and 0.33 at.% in 0.75NB2.75S [13]. Solubility limits of Cr^{VI} are higher and therefore the Cr_2O_3 layer seems to dissolve into Cr^{III} entities. On the other hand, the diffusion lengths in Fig. 5 are more consistent with the diffusion of Cr^{VI}. Taking the N3S melt as example, the calculated diffusion length after 51 h and considering Cr^{VI} ($x = 2\sqrt{Dt}$) is about 300 µm which is consistent with the measured

profile, while calculations considering Cr^{III} give millimetre-sized diffusion length which is far too high. Diffusion coefficients are taken from [13] and listed in Table 1.

Experimental results in the melts allow different interpretations about the diffusing species. In order to discriminate which specie (Cr^{III} or Cr^{VI}) diffuses in the melt, modelling of the Cr-consumption and depletion profiles in the alloy is used. Indeed, for a given oxide thickness, to comply with the mass balance, the chromium depletion in the alloy would be more significant with a Cr^{III} diffusion process in the melt due to its higher diffusivity. The following equations, considering a total interface recession for the alloy, are used to model the depletion of chromium in the alloy [12,40,41]:

$$N_{\mathrm{Cr\,(x,t)}} = N_{\mathrm{Cr}}^{\mathrm{i}} + \left(N_{\mathrm{Cr}}^{\circ} - N_{\mathrm{Cr}}^{\mathrm{i}}\right) \frac{\mathrm{erf}\left(\frac{x+\sqrt{2k_{\mathrm{c}}t}}{2\sqrt{\widetilde{D}_{\mathrm{Ni-Cr}}t}}\right) - \mathrm{erf}\left(\sqrt{\frac{k_{\mathrm{c}}}{2\widetilde{D}_{\mathrm{Ni-Cr}}}}\right)}{\mathrm{erfc}\left(\sqrt{\frac{k_{\mathrm{c}}}{2\widetilde{D}_{\mathrm{Ni-Cr}}}}\right)} \qquad \text{Equation 4}$$

with

$$\frac{N_{\mathrm{Cr}}^{\circ} - N_{\mathrm{Cr}}^{\mathrm{i}}}{1 - N_{\mathrm{Cr}}^{\mathrm{i}}} = \mathrm{F}\left(\sqrt{\frac{k_{\mathrm{c}}}{2\widetilde{D}_{\mathrm{Ni-30Cr}}}}\right) \qquad \text{Equation 5}$$

F is a function defined by $F(u) = \pi^{-1/2}u(1-\mathrm{erf}\,u)\exp(u^2)$. N_{Cr}° is the atomic fraction of chromium in the core of the alloy, N_{Cr}^{i} is the atomic fraction at the alloy/oxide interface, and $\tilde{D}_{\mathrm{Ni\text{-}30Cr}}$ is the interdiffusion coefficient of chromium in the Ni-30Cr alloy, taken as 1.2 x 10^{-10} cm^2 s^{-1} [12]. t is the time in s and x the depth in the alloy in cm. k_c is the parabolic constant rate for the recession of the alloy/oxide interface in cm^2 s^{-1}. This constant is given by Eq. 6 in the case of simultaneous oxidation and dissolution of the oxide layer as demonstrated by Gheno and Gleeson [42]:

$$k_{\mathrm{c}} = \left(2\frac{V_{\mathrm{Ni-30Cr}}}{V_{\mathrm{Cr_2O_3}}}\right)^2 \frac{{k_{\mathrm{p}}}^2}{g} \qquad \text{Equation 6}$$

$V_{\mathrm{Ni\text{-}30Cr}}$ and V_{Cr2O3} are the molar volumes of the alloy and the oxide in cm^3 mol^{-1} respectively. k_p is the parabolic constant for pure oxidation (in the absence of oxide dissolution) in cm^2 s^{-1}. g is the parabolic constant (in cm^2 s^{-1}) for the oxide growth in the melt in the absence of initial oxide thickness (Eq. 2). In this approach, the approximation of assimilating the two initial hours of preoxidation to corrosion in silicate melt is made. This approximation leads to an overestimation of the chromium depletion in the alloy, more significant for short term immersions or high dissolution rates.

The chromium depletion profiles in Ni-30Cr alloy at 1150°C calculated with Eq. 4 to 6 for the oxide formation without dissolution, and with dissolution controlled by either a Cr^{III} or a Cr^{VI} diffusion process are shown in Fig. 5 a, b and c and compared with the experimental depletion profiles after 2 h of preoxidation followed by 51 h, 2 h and 25 h of immersion in N3S, 2.3NB5S and 0.75NB2.75S melts respectively. Values for S_{CrIII}, D_{CrIII} and D_{CrVI} are taken from Table 1. Modelling considering a Cr^{III} diffusion process leads to much higher chromium depletions than the experimental ones, while the modelling considering Cr^{VI} diffusion is in good agreement with experimental depletion (Fig. 6). Moreover, an interfacial chromium content would be about 5 wt.% in the case of Cr^{III} diffusion in the 0.75NB2.75S (Fig. 6b). This is too low to sustain the external growth of the oxide and internal oxidation should occur [43]. Modelling considering Cr^{III} diffusion in the 2.3NB5S melt (Fig. 6c) leads to negative chromium contents when approaching the alloy/oxide interface. Negative values are obviously not realistic, so these modelling do not support the hypothesis of a Cr^{III} diffusion process. In the case of silicate melt N3S, the modelled depletion is less steep, but yet not satisfactory either when compared with the experimentally measured profile. However, when modelling depletion profiles with a Cr^{VI} diffusion process, a good agreement is found with experimental profiles for all melts. It is also noticeable that the oxidation-dissolution with Cr^{VI} diffusion process actually induces only a small extent on the depletion profiles compared to pure oxidation. This means that the presence of the melt does not seem too detrimental for the alloy lifetime in a passive steady-state regime, especially for viscous melts.

To conclude, the modelling of chromium depletion profiles in Fig. 6 allows concluding that Cr^{VI} species are limiting the diffusion of chromium through the melts. The following mechanisms for the dissolution of the Cr_2O_3 layer can be proposed: firstly, Cr_2O_3 undergoes an acid-base dissolution reaction at the oxide/melt interface into Cr^{III} species, as attested by the reaching of its solubility limit at the oxide/melt interface. When leaving the interface, Cr^{III} is oxidised into Cr^{VI} because of the high redox of the melts equilibrated in air [8,34]. Even if equilibrium between Cr^{III} and Cr^{VI} species is still existing [3,4,44], Cr^{VI} oxo-complexes (CrO_4^{2-}) are likely to be larger than Cr^{III} species [14,15]. As a consequence, the percolation pathways in the melts would be saturated with Cr^{VI} oxo-complexes which impose their diffusion kinetics [45].

5. Kinetic modeling of the oxide layer growth

In this section, an analytic and numeric resolution of the growth rate of the oxide layer is developed.

5.1. Analytical solution

The formation rate of the oxide layer is assimilated to its parabolic kinetics in gas atmosphere; therefore it is given by Eq. 7 [46]. It has been previously demonstrated that the dissolution of the oxide layer is kinetically limited by the diffusion of chromium species in the melt, a semi-infinite media. Thus, the dissolution rate can be expressed by Eq. 8 [47].

$$\left(\frac{\mathrm{d}x}{\mathrm{d}t}\right)_{\mathrm{f}} = \frac{k_{\mathrm{p}}}{x} \qquad \text{Equation 7}$$

$$\left(\frac{\mathrm{d}x}{\mathrm{d}t}\right)_{\mathrm{d}} = -\frac{M_{\mathrm{Cr_2O_3}}}{\rho_{\mathrm{Cr_2O_3}}} S_{Cr} \sqrt{\frac{D_{\mathrm{Cr}}}{\pi t}} = -\frac{k_{\mathrm{d}}}{\sqrt{t}} \qquad \text{Equation 8}$$

Where $\left(\frac{\mathrm{d}x}{\mathrm{d}t}\right)_{\mathrm{f}}$ and $\left(\frac{\mathrm{d}x}{\mathrm{d}t}\right)_{\mathrm{d}}$ are the rate for pure formation and for dissolution of the oxide layer respectively. k_{p} is the parabolic rate constant of oxidation (in $cm^2\ s^{-1}$) and x is the Cr_2O_3 layer thickness (in cm), M_{Cr2O3} and ρ_{Cr2O3} are the molar weight (in $g\ mol^{-1}$) and the density (in $g\ cm^{-3}$) of chromia respectively. S_{Cr} and D_{Cr} are the chromium solubility limit (in $mol\ cm^{-3}$) and diffusion coefficient (in $cm^2\ s^{-1}$) in the silicate melt. k_{d} refers to the dissolution rate constant expressed in $cm\ s^{-1/2}$.

The variation of the oxide layer thickness in silicate melts is obtained by the combination of its formation and its dissolution rates and is expressed by Eq. 9.

$$\frac{\mathrm{d}x}{\mathrm{d}t} = \left(\frac{\mathrm{d}x}{\mathrm{d}t}\right)_{f} + \left(\frac{\mathrm{d}x}{\mathrm{d}t}\right)_{\mathrm{d}} = \frac{k_{\mathrm{p}}}{x} - \frac{k_{\mathrm{d}}}{\sqrt{t}} \qquad \text{Equation 9}$$

Considering the following substitution of variable and its derivate form (Eq. 10 and 11):

$$\alpha = \frac{x}{\sqrt{t}} \qquad \text{Equation 10}$$

$$\frac{\mathrm{d}x}{\mathrm{d}t} = \sqrt{t}\frac{\mathrm{d}\alpha}{\mathrm{d}t} + \frac{\alpha}{2\sqrt{t}}$$ Equation 11

By substitution with Eq. 11, Eq. 9 becomes:

$$t\frac{\mathrm{d}\alpha}{\mathrm{d}t} = \frac{-\frac{1}{2}\alpha^2 - k_\mathrm{d}\alpha + k_\mathrm{p}}{\alpha}$$ Equation 12

The solutions of the polynomial at the numerator of Eq. 12 are:

$$\alpha^{\pm} = -k_\mathrm{d} \pm \sqrt{{k_\mathrm{d}}^2 + 2k_\mathrm{p}}$$ Equation 13

It is noteworthy to notice that $\alpha^+ = \sqrt{(2g^-)}$ and $\alpha^- = -\sqrt{(2g^+)}$, involving the two mathematical solutions of Eq. 9, considering $x^2 = 2g^{\pm}t$ and $g^{\pm} = k_\mathrm{d}^2+k_\mathrm{p}\pm k_\mathrm{d}\sqrt{(k_\mathrm{d}^2+k_\mathrm{p})}$ and g^- being the global growth constant g presented in the introduction (Eq. 2), the particular law for oxide growth with no initial layer.

Then, Eq. 12 can be written in the factorised form (Eq. 14):

$$-\frac{1}{2t}dt = \frac{\alpha}{(\alpha-\alpha^-)(\alpha-\alpha^+)}d\alpha$$ Equation 14

Which can be transformed into a usual integration formula (Eq. 15):

$$-\frac{1}{2}\int\frac{1}{t}dt = \int\left(\frac{A}{(\alpha-\alpha^+)} + \frac{B}{(\alpha-\alpha^-)}\right)d\alpha$$ Equation 15

With:

$$\mathrm{A} = \frac{\alpha^+}{\alpha^+ - \alpha^-}$$ Equation 16

$$\mathrm{B} = \frac{\alpha^-}{\alpha^- - \alpha^+}$$ Equation 17

The integration of Eq. 15 gives:

$$C + A\ln(\alpha-\alpha^+) + B\ln(\alpha-\alpha^-) + \frac{1}{2}\ln t = 0$$ Equation 18

With C being the integration constant. Considering the case of a negligible dissolution (*i.e.* $k_d = 0$), this integration constant can be easily found and is equal to -ln x_0, with x_0 the initial oxide layer thickness. Therefore, after development, the solution for Eq. 9 is, with t and $x \neq 0$:

$$\left(1 - \frac{k_d}{\sqrt{{k_d}^2 + 2k_p}}\right) \ln\left(\frac{x}{\sqrt{t}} - \sqrt{2g^-}\right) + \left(1 + \frac{k_d}{\sqrt{{k_d}^2 + 2k_p}}\right) \ln\left(\frac{x}{\sqrt{t}} + \sqrt{2g^+}\right) + \ln t - 2\ln x_0 = 0 \quad \text{Equation 19}$$

Eq. 19 is the general solution for the evolution of the oxide layer thickness subjected to a parabolic formation and a simultaneous dissolution in a semi-infinite media. This expression depends on the rate constants of formation and dissolution of the oxide layer k_p and k_d. For any value of x, the value for t that fulfils Eq. 19 can be obtained graphically or with a calculation software.

5.2. Numerical resolution

The equation of the oxide thickness growth (Eq. 9) can also be solved with the numerical Euler's method:

$$x(t + \Delta t) = x(t) + \frac{\mathrm{d}x}{\mathrm{d}t}(t)\Delta t \quad \text{Equation 20}$$

By choosing an adequate time step Δt, the differential equation (Eq. 9) can be solved accurately.

Calculations of the evolution of the Cr_2O_3 layer thickness with Eq. 20 have been performed and are presented on Fig. 7 a, b and c for each melt. The time step Δt used for calculations is 10 s. Experimental data and calculations with Eq. 19 are also shown for the sake of comparison. On Fig. 7, calculations with analytical and numerical methods are shown considering diffusion of Cr^{III} or Cr^{VI} in the melts.

First of all, a perfect agreement is observed between the results obtained from numerical and analytical calculations. This means that the time step chosen for the Euler's

method is small enough and this agreement gives an assurance of reliability for the intricate analytical solution (Eq. 19). In all calculations, the oxide thickness evolution displays a local minimum shortly after immersion. This is the consequence of the small growth rate – because of the presence of the initial oxide – compared to the high dissolution rate for short time, so $k_p/x < k_d/\sqrt{t}$ in Eq. 9 and a decrease of the calculated oxide thickness is first observed after immersion in the melts. Moreover, the difference of three orders of magnitude between the diffusion coefficients of Cr^{III} and Cr^{VI} causes a stronger initial decrease for the Cr^{III} curve and a gap of a few microns over time between Cr^{III} and Cr^{VI} curves.

For the three melts, a good agreement is found between experimental data and the oxide thickness calculated considering the diffusion coefficient of Cr^{VI}. This agreement confirms that the diffusion of Cr^{VI} species in the silicate melts limits the chromia dissolution rate as previously evidenced. Furthermore, it should be emphasised that, since both formation and dissolution are diffusion controlled processes, the long-term evolution of the oxide thickness exhibits a parabolic behaviour as it has been shown by Gheno and Lindwall [23]. The Cr^{VI} diffusion process is certainly responsible for the good behaviour of Ni-Cr alloy in simple silicate melts, as it induces only a small chromium overconsumption from the alloy due to the limited dissolution rate. A Cr^{III} diffusion process would drag too much chromium from the alloy making the continuous formation of the external Cr_2O_3 layer impossible, as the chromium diffusion within the alloy would become the limiting step. Such Cr^{III} diffusion process could be found in glass melts equilibrated in low oxygen atmospheres, e.g. in argon or nitrogen when the glass redox becomes lower than the Cr^{VI}/Cr^{III} redox potential. Deviations of the experimental results from the simulation can be explained by various reasons. Some are given hereafter in a non-exhaustive list: the temperature distribution in the furnace causes discrepancies on the preoxidation thickness ; the dissolution of alumina can affect both the solubility of chromium and its diffusivity by changing the viscosity of the melt ; the value of the parabolic constant k_p for the oxide formation actually decreases during the first hours before reaching a steady value, so the oxide thickness can be underestimated [28].

6. Conclusions

A thorough identification of the mechanisms involved in the formation-dissolution processes of protective chromia layers led to analytical description of the corrosion kinetics of chromium-rich alloys in molten silicates. The chromium from the alloy reacts with dissolved

oxygen from the melt to sustain the oxide formation, while the oxide is dissolved into Cr^{III} in the melt via an acid-base reaction. Then Cr^{III} is oxidised into Cr^{VI} within the melt due to the high potential of the liquid. Eventually Cr^{VI} diffuses into the melt. Consequently, the dissolution reaction of chromia is limited by the diffusion of the Cr^{VI} species through the melt. A successful modelling has been achieved without any fitting. Parameters of the modelling were independently and experimentally obtained. These parameters are the parabolic rate constant for the oxidation of the alloy, the solubility limit of Cr^{III} and diffusion coefficient of Cr^{VI} the melt.

In some cases, a depassivation phenomenon with total dissolution of the oxide layer occurs, particularly in aggressive glass melt or when increasing temperature [13,24,48]. The present model does not mathematically predict such phenomenon characterised by a drop of the oxide thickness to zero. The model is based on the static hypotheses that supplies of chromium from the alloy and oxygen in the melt are able to sustain the Cr_2O_3 growth. So, even if the origins of the depassivation are still unclear at this day, they may come from a lack in the chromium supply from the alloy or in the oxygen supply from the melt.

Data availability

The raw/processed data required to reproduce these findings cannot be shared at this time as the data also forms part of an ongoing study.

References

[1] L.J. Manfredo, R.N. McNally, Solubility of Refractory Oxides in Soda-Lime Glass, J. Amer. Ceram. Soc. 67 (1984) C155-C158. https://doi.org/10.1111/j.1151-2916.1984.tb19178.x

[2] C.W. Kim, K. Choi, J.K. Park, S.W. Shin, M.J. Song, Enthalpies of chromium oxide solution in soda lime borosilicate glass systems, J. Am. Ceram. Soc. 84 (2001) 2987-2990. https://doi.org/10.1111/j.1151-2916.2001.tb01125.x

[3] H. Khedim, R. Podor, C. Rapin, M. Vilasi, Redox-control solubility of chromium oxide in soda-silicate melts, J. Am. Ceram. Soc. 91 (2008) 3571–3579. https://doi.org/10.1111/j.1551-2916.2008.02692.x

[4] H. Khedim, R. Podor, P.J. Panteix, C. Rapin, M. Vilasi, Solubility of chromium oxide in binary soda-silicate melts, J. Non-Cryst. Solids 356 (2010) 2734-2741. https://doi.org/10.1016/j.jnoncrysol.2010.09.045

[5] H. Khedim, S. Abdelouhab, R. Podor, C. Rapin, M. Vilasi, P.J. Panteix, M. Toplis, F. Faure, Kinetic and equilibrium factors affecting saturation of chromium oxide in soda-silicate melts, J. Non-Cryst. Solids, 357 (2011) 31–42. https://doi.org/10.1016/j.jnoncrysol.2010.10.012

[6] T.K. Abdullah, C. Petitjean, P.J. Panteix; C. Rapin, M. Vilasi, Z. Hussain, A.A. Rahim, Stability of Protective Oxide Layer Against Corrosion: Solubility Measurements of Chromium in Soda Lime Silicate Melts, Oxid. Met. 80 (2013) 611-622. https://doi.org/10.1007/s11085-013-9400-4

[7] H. Zhu, Q. Liao, F. Wang, Y. Dai, M. Lu, The effects of chromium oxide on the structure and properties of iron borophosphate glasses, J. Non-Cryst. Solids 437 (2016) 48-52. https://doi.org/10.1016/j.jnoncrysol.2016.01.013

[8] J. Di Martino, C. Rapin, P. Berthod, R. Podor, P. Steinmetz, Corrosion of metals and alloys inmoltenglasses. Part1: glass electrochemical properties and pure metal (Fe, Co, Ni, Cr) behaviours, Corros. Sci. 46 (2004) 1849–1864. https://doi.org/10. 1016/j.corsci.2003.10.024

[9] J. Di Martino, C. Rapin, P. Berthod, R. Podor, P. Steinmetz, Corrosion of metals and alloys in molten glasses. Part 2: nickel and cobalt high chromium superalloys behaviour and protection, Corros. Sci. 46 (2004) 1865–1881. https://doi.org/10. 1016/j.corsci.2003.10.025

[10] P. Sengupta, J. Mittra, G.B. Kale, Interaction between borosilicate melt and Inconel, J. Nucl. Mater. 350 (2006) 66-73. https://doi.org/10.1016/j.jnucmat.2005.11.012

[11] P. Sengupta, C.P. Kaushik, G.B. Kale, D. Das, K. Raj, B.P. Sharma, Evaluation of alloy 690 process pot at the contact with borosilicate melt pool during vitrification of high-level nuclear waste, J. Nucl. Mater. 392 (2009) 379-385. https://doi.org/10.1016/j.jnucmat.2008.07.046

[12] E. Schmucker, C. Petitjean, P.J. Panteix, L. Martinelli, S. Ben Lagha, M. Vilasi, Oxidation of Ni-Cr alloy at intermediate oxygen pressures. II. Towards the lifetime prediction of alloys, Corros. Science 111 (2016) 467-473. https://doi.org/10.1016/j.corsci.2016.05.024

[13] E. Schmucker, C. Petitjean, P.-J. Panteix, L. Martinelli, S. Ben Lagha, M. Vilasi, Correlation between chromium physicochemical properties in silicate melts and the corrosion behavior of chromia-forming alloy, J. Nucl. Mater. 510 (2018) 100–108. https://doi.org/10.1016/j.jnucmat.2018.07.059

[14] H.D. Schreiber, L.A. Haskin, Chromium in basalts: experimental determination of redox states and partinioning among synthetic silicate phases, Proc. Lunar. Sci. Conf. 7 (1976) 1221-1259.

[15] O. Villain, Contribution à l'étude de l'environnement structural du chrome dans les verres, thèse de l'Université Pierre et Marie Curie, 2009, Paris. https://tel.archives-ouvertes.fr/tel-00406764

[16] A.J. Berry, H.S.C. O'Neill, D.R. Scott, G.J. Foran, J.M.G. Shelley, The effect of composition on Cr^{2+}/Cr^{3+} in silicate melts, Amer. Mineral. 91 (2006) 1901-1908. https://doi.org/10.2138/am.2006.2097

[17] O. Claussen, C. Rüssel, Self diffusion of polyvalent ions in a borosilicate melt, J. Non-Cryst. Solids, 215 (1997) 68-74. https://doi.org/10.1016/S0022-3093(97)00036-7

[18] O. Claussen, C. Rüssel, Diffusivities of polyvalent elements in glass melts, Solid State Ion. 105 (1998) 289-296. https://doi.org/10.1016/S0167-2738(97)00476-1

[19] O. Claußen, S. Gerlach, C. Rüssel, Self-diffusivity of polyvalent ions in silicate liquids. J. Non-Cryst. Solids, 253 (1999) 76-83. https://doi.org/10.1016/S0022-3093(99)00345-2

[20] G. von der Gönna, C. Rüssel, Diffusivities of polyvalent elements in a $15Na_2O$-$85SiO_2$ glass melt, J. Non-Cryst. Solids, 272 (2000) 139-146. https://doi.org/10.1016/S0022-3093(00)00234-9

[21] G. von der Gönna, C. Rüssel, Diffusivities of various polyvalent elements in a Na_2O-$2SiO_2$ glass melt, J. Non-Cryst. Solids, 272 (2000) 139-146. https://doi.org/10.1016/S0022-3093(99)00598-0

[22] J. Vondrak, D. Rohanova, B. Klapste, J. Velicka, Voltammetric measurement of the Pt electrode capacity and the determination of the polyvalent ions diffusion coefficients in the glass melt, Ceram.-Silik. 47 (2003) 51-55.

[23] T. Gheno, G. Lindwall, On the Simulation of Composition Profiles in NiCoCrAl Alloys During Al_2O_3 Scale Growth in Oxidation and Oxidation-Dissolution Regimes, Oxid. Met. 91 (2019) 243-257. https://doi.org/10.1007/s11085-018-9877-y

[24] T. Gheno, G.H. Meier, B. Gleeson, High Temperature Reaction of MCrAlY Coating Compositions with CaO Deposits, Oxid. Met. 84 (2015) 185-2099. https://doi.org/10.1007/s11085-015-9550-7

[25] Y. Xu, W. Li, X. Yang, Influence of alloyed Fe on corrosion of Ni-Cr alloys in molten silicates and the effects of pre-oxidation treatment, Corros. Sci. 134 (2018) 179-188. https://doi.org/10.1016/j.corsci.2018.02.022

[26] T. K. Abdullah, C. Petitjean, P.J. Panteix, E. Schmucker, C. Rapin, M. Vilasi, Corrosion of pure Cr and Ni–30Cr alloy by soda–lime–silicate melts: study of simplified systems, Oxidation of Metals 85 (2016) 3-16. https://doi.org/10.1007/s11085-015-9571-2

[27] Y. Xu, J. Yan, F. Sun, Y. Gu, Effect of alloyed Al on the corrosion behavior of Ni-base alloys in molten glass under static condition, Corros. Sci. 112 (2016) 635-646. http://dx.doi.org/10.1016/j.corsci.2016.09.006

[28] Y. Xu, J. Yan, F. Sun, A. Ikeda, Y. Gu, Effect of further alloying elements on corrosion resistance of Ni-Cr alloys in molten glass, Corros. Sci. 112 (2016) 647-656. http://dx.doi.org/10.1016/j.corsci.2016.09.007

[29] E. Schmucker, C. Petitjean, P.J. Panteix, L. Martinelli, S. Ben Lagha, M. Vilasi, Oxidation of Ni-Cr alloy at intermediate oxygen pressures. I. Diffusion mechanisms through the oxide layer, Corros. Science 111 (2016) 474-485. https://doi.org/10.1016/j.corsci.2016.05.025

[30] F. Autefage, J.J. Couderc, Etude du mécanisme de la migration du sodium et du potassium au cours de leur analyse à la microsonde électronique, Bull. Mineral. 103 (1980) 623-629.

[31] C. Desgranges, F. Lequien, E. Aublant, M. Nastar, D. Monceau, Depletion and Voids Formation in the Substrate During High Temperature Oxidation of Ni-Cr Alloys, Oxid. Met. 79 (2013) 93-105. https://doi.org/10.1007/s11085-012-9328-0

[32] D. Lizarazu, P. Steinmetz, J.L. Bernard, Corrosion of nickel-chromium alloys by molten glass at 1100°C: An electrochemical study, Mater. Sci. Forum 251 (1997) 709-722. https://doi.org/10.4028/www.scientific.net/MSF.251-254.709

[33] A. Carton, C. Rapin, R. Podor, P. Berthod, Corrosion of chromium in glass melts, J. Electrochem. Soc. 153 (2006) 121-127. https://doi.org/10.1149/1.2165745

[34] C. Petitjean, P.J. Panteix, C. Rapin, M. Vilasi, R. Podor, Electrochemical behavior of glass melts: application to corrosion processes, Procedia Materials Science 7 (2014) 101–110. https://doi.org/10.1016/j.mspro.2014.10.014

[35] J.T. Wenzel, D.M. Sanders, Sodium and boron vaporisation from a boric oxide and a borosilicate glass melt, Phys. Chem. Glasses, 23 (1982) 47-52.

[36] M. Cable, M.H.V. Fernandes, The volatilization of sodium metaborate, Glass Technol. 28 (1987) 135-140.

[37] E. Schmucker, Compréhension et modélisation des mécanismes de corrosion des alliages chromino-formeurs dans les verres nucléaires, Thèse de l'Université de Lorraine, 2016, Nancy. https://tel.archives-ouvertes.fr/tel-01503906

[38] E. Essuman, G.H. Meier, J. Zurek, M. Hänsel, T. Norby, L. Singheiser, W.J. Quadakkers, Protective and non-protective scale formation of NiCr alloys in water vapour containing high- and low-pO_2 gases, Corros. Sci. 50 (2008) 1753-1760. https://doi.org/10.1016/j.corsci.2008.03.001

[39] P. Gateau, C. Petitjean, P.J. Panteix, C. Rapin, M. Vilasi, Tin oxide solubility in soda-lime-silica melts, Phys. Chem. Glasses: Eur. J. Glass Sci. Technol. B 53 (2012) 68-73.

[40] C. Wagner, Theoretical analysis of the diffusion processes determining the oxidation rate of alloys, J. Electrochem. Soc. 99 (1952) 772-782. https://doi.org/10.1149/1.2779605

[41] B.D. Bastow, D.P. Whittle, G.C. Wood, Alloy depletion profiles resulting from the preferential removal of the less noble metal during alloy oxidation, Oxid. Met. 12 (1978) 413-438. https://doi.org/10.1007/BF00612088

[42] T. Gheno, B. Gleeson, Kinetics of Al2O3-Scale Growth by Oxidation and Dissolution in Molten Silicate, Oxid. Met. 87 (2017) 527-539. https://10.1007/s11085-016-9686-0

[43] A. Prilleux, D. Jullian, J. Zhang, D. Monceau, D.J. Young, Internal Oxidation in Dry and Wet Conditions for Oxygen Permeability of Fe-Ni Alloys at 1150 and 1100 °C, Oxid. Met. 87 (2017) 273-283. https://doi.org/10.1007/s11085-017-9724-6

[44] Y.A. Guloyan, Kinetics of Chromium Oxide Transformations in Glass Melting, Glass Ceram+ 62 (2005) 231-234. https://doi.org/10.1007/s10717-005-0079-0

[45] G.N. Greaves, EXAFS, glass structure and diffusion, Philos. Mag. B 60 (1989) 793-800. https://doi.org/10.1080/13642818908209743

[46] D.J. Young, High Temperature Oxidation and Corrosion of Metals, Elsevier, Amsterdam, 2008.

[47] J. Crank, The mathematics of diffusion, Clarendon Press, Oxford, 1975.

[48] V. Szczepan, C. Petitjean, P.J. Panteix, M. Vilasi, Corrosion and depassivation of a chromia-forming Ni-based alloy in the $0.75Na_2O$-B_2O_3-$2.75SiO_2$ melt, Corros. Sci. (2020) in press. https://doi.org/10.1016/j.corsci.2020.108579

Figure Captions

Figure 1: Cross-section BSE micrograph of the Ni-30Cr alloy surface after preoxidation treatment at 1150 °C during 2 h above the glass batch.

Figure 2: Cross-section BSE micrographs of the preoxidised Ni-30Cr/glass melt interface after immersion at 1150 °C in (a) N3S melt during 51 h; (b) 0.75NB2.75S melt during 25 h and (c) 2.3NB5S during 2 h.

Figure 3: Oxide thickness evolutions on the preoxidised Ni-30Cr alloy immersed at 1150 °C in a) N3S melt; b) 0.75NB2.75S melt and c) 2.3NB5S melt. Immersion durations are indicated next to the points. The first point corresponds to the preoxidised sample without immersion.

Figure 4: Chromium depletion profiles in preoxidised Ni-30Cr alloy after immersions at 1150 °C in a) N3S melt; b) 0.75NB2.75S and c) 2.3NB5S.

Figure 5: Chromium concentration profiles from the oxide/glass interface after immersions of the preoxidised alloy at 1150°C for several durations.

Figure 6: Experimental and calculated chromium depletion profiles in the alloy at after corrosion in a) N3S melt: 2 h preoxidation + 51 h immersion (green dots – exp.), pure oxidation 53 h (black line – calc.), pure corrosion Cr^{III} process 53 h (purple dashes – calc.) and pure corrosion Cr^{VI} process 53 h (orange dashes – calc.) ; b) 0.75NB2.75S melt: 2 h preoxidation + 25 h immersion (blue dots – exp.), pure oxidation 27 h (black line – calc.), pure corrosion Cr^{III} process 27 h (purple dashes – calc.) and pure corrosion Cr^{VI} process 27 h (orange dashes – calc.) and c) 2.3NB5S melt: 2 h preoxidation + 2 h immersion (red dots – exp.), pure oxidation 4 h (black line – calc.), pure corrosion Cr^{III} process 4 h (purple dashes – calc.) and pure corrosion Cr^{VI} process 4 h (orange dashes – calc.)

Figure 7: Modelling of the oxide thickness evolution on Ni-30Cr immersed at 1150 °C with analytical and numerical methods for Cr^{III} and Cr^{VI} diffusion processes in a) N3S melt, b) 0.75NB2.75S melt and c) 2.3NB5S melt.

Table 1: Theoretical and measured compositions (mol.%) and physicochemical properties of the glasses at 1150°C [13].

		N3S	2.3NB5S	0.75NB2.75S
Na_2O	th.	25	28	16.69
	exp.	23.30 ± 0.31	26.28 ± 0.39	16.78 ± 0.23
B_2O_3	th.	-	12	22.23
	exp.	-	13.11 ± 0.30	22.54 ± 0.54
SiO_2	th.	75	60	61.08
	exp.	76.70 ± 0.14	60.61 ± 0.54	60.68 ± 0.54
Optical basicity (Λ)		0.57	0.56	0.52
Viscosity (log η(dPa s))		2.89 - 2.97	1.42 – 1.98	1.57 - 2.09
Density ρ (g cm^{-3})		2.24	2.20	2.17
$S(Cr^{III})$ (mol cm^{-3})		5.1×10^{-4} (0.45at.%)	5.1×10^{-4} (0.45at.%)	3.9×10^{-4} (0.33at.%)
$D(Cr^{III})$ (cm^2 s^{-1})		1.4×10^{-7}	5.0×10^{-6}	1.5×10^{-6}
$D(Cr^{VI})$ (cm^2 s^{-1})		1.3×10^{-9}	1.1×10^{-7}	2.5×10^{-8}

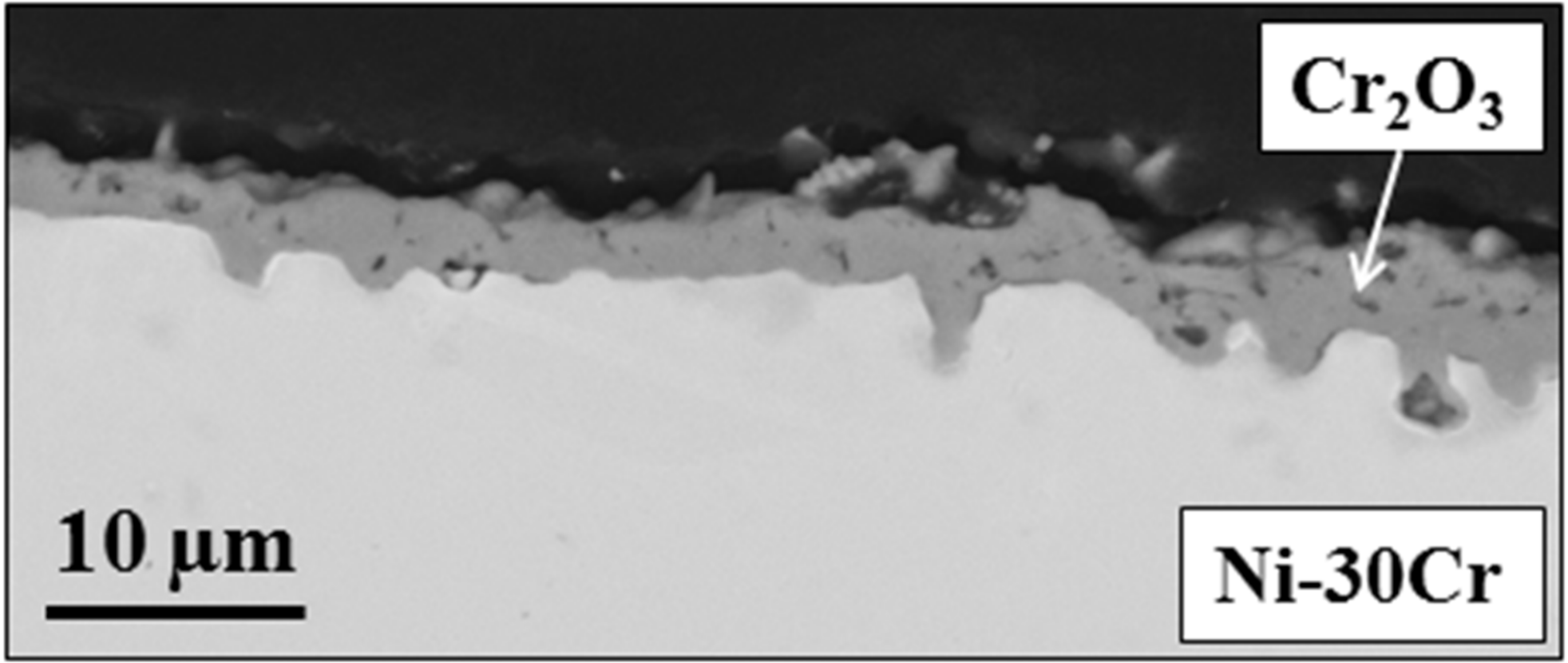
Cr_2O_3
10 µm
Ni-30Cr

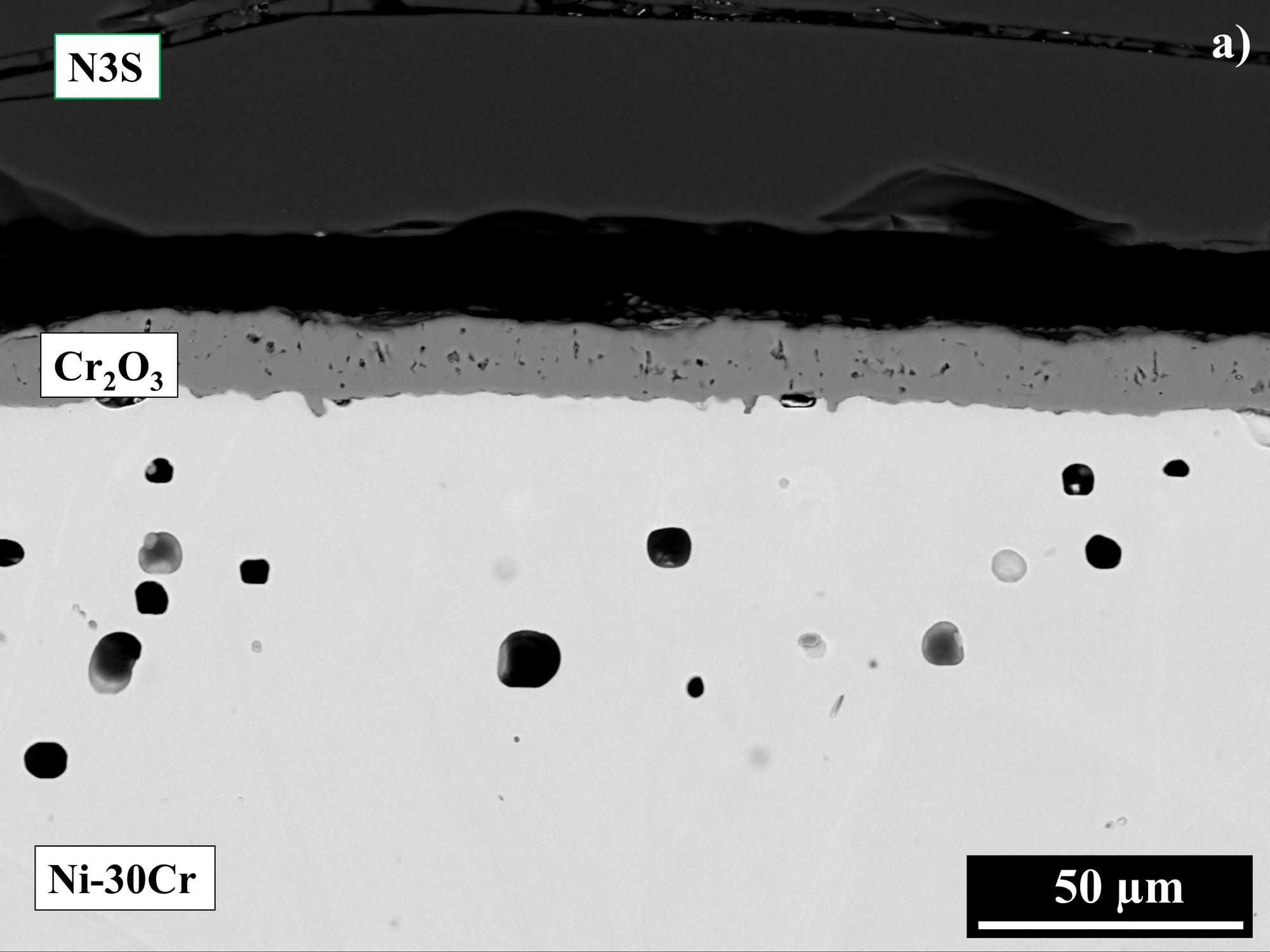
a)
N3S
Cr_2O_3
Ni-30Cr
50 µm

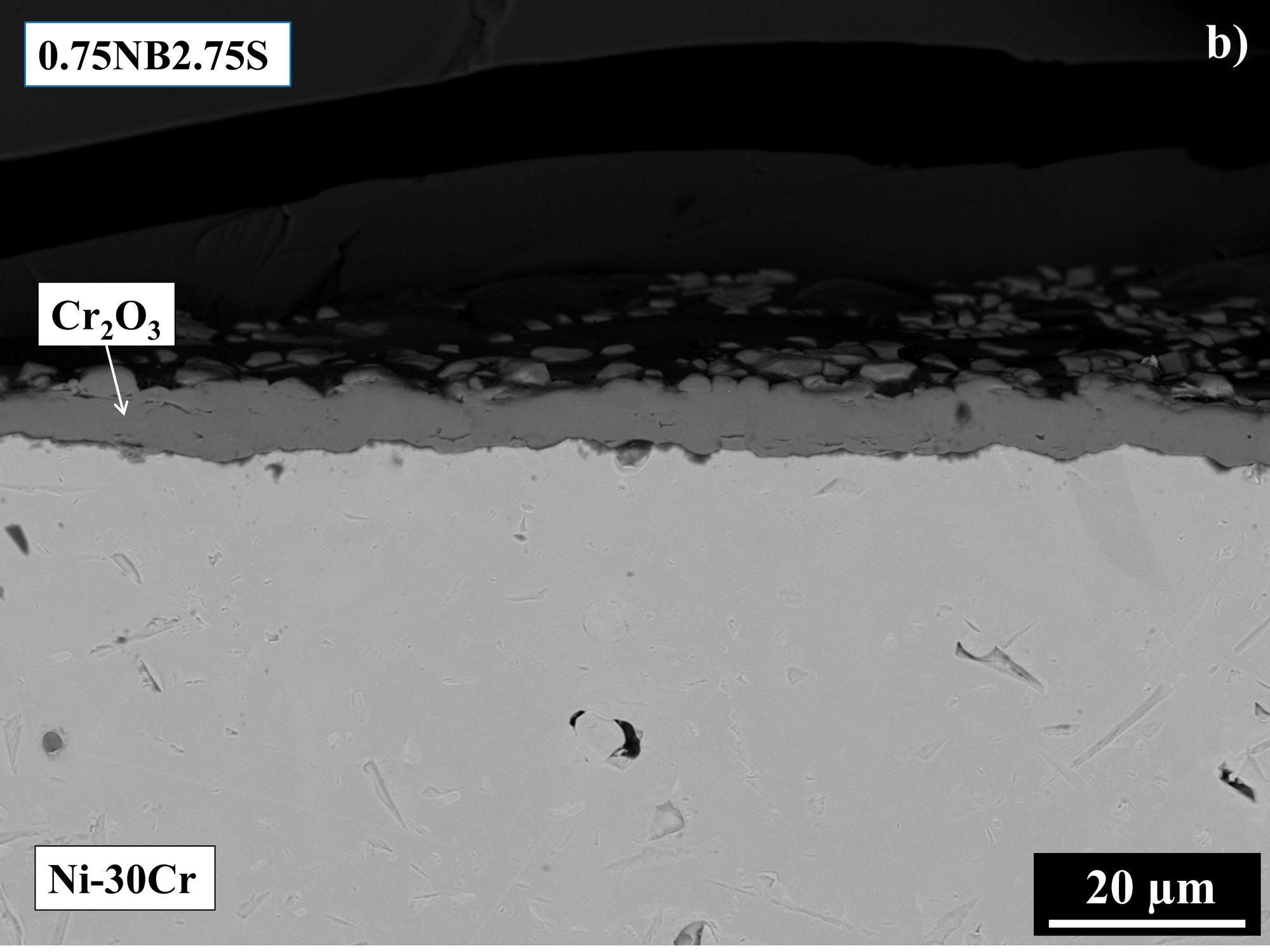
0.75NB2.75S
b)
Cr_2O_3
Ni-30Cr
20 µm

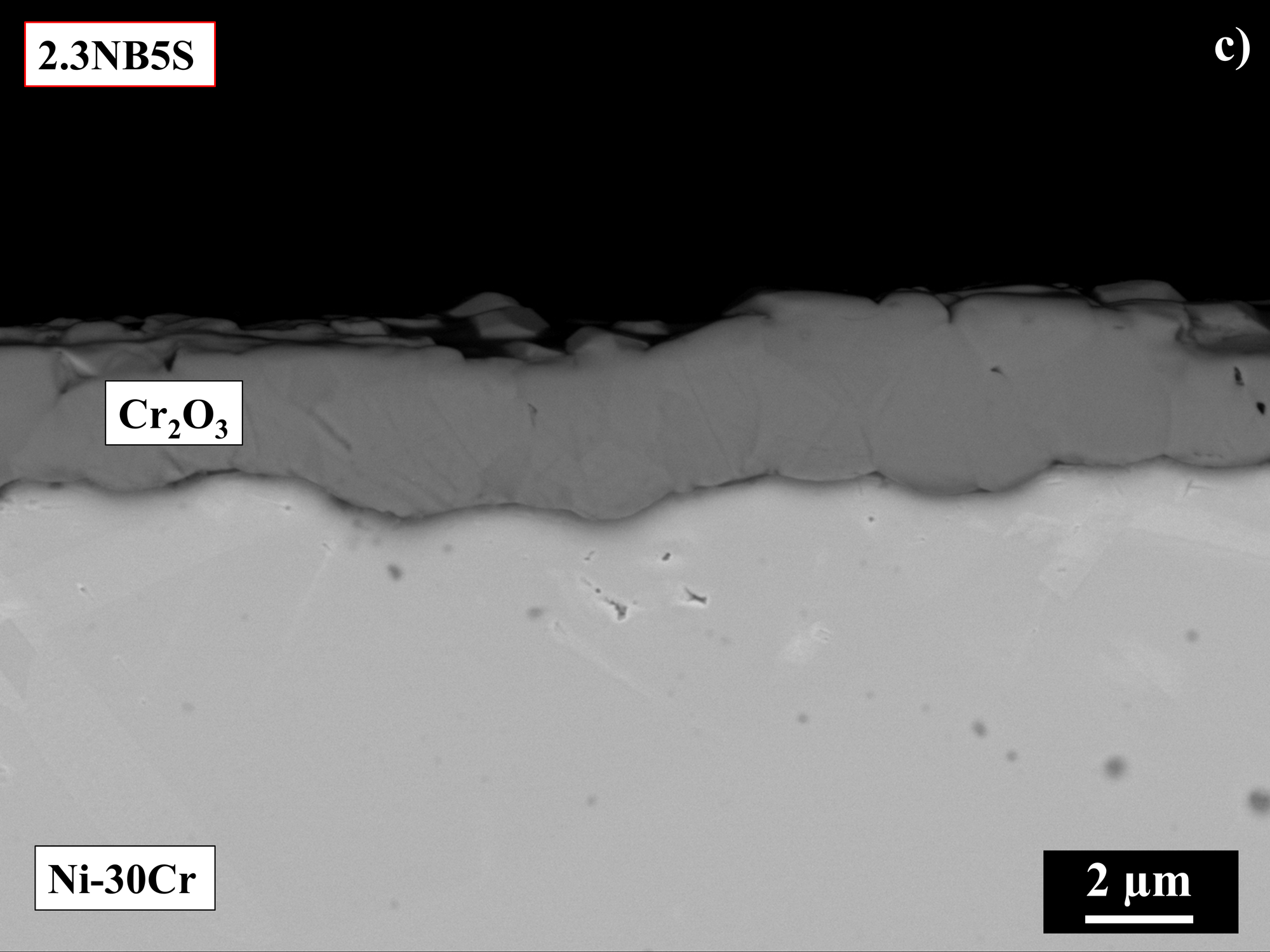
2.3NB5S
c)
Cr_2O_3
Ni-30Cr
2 µm

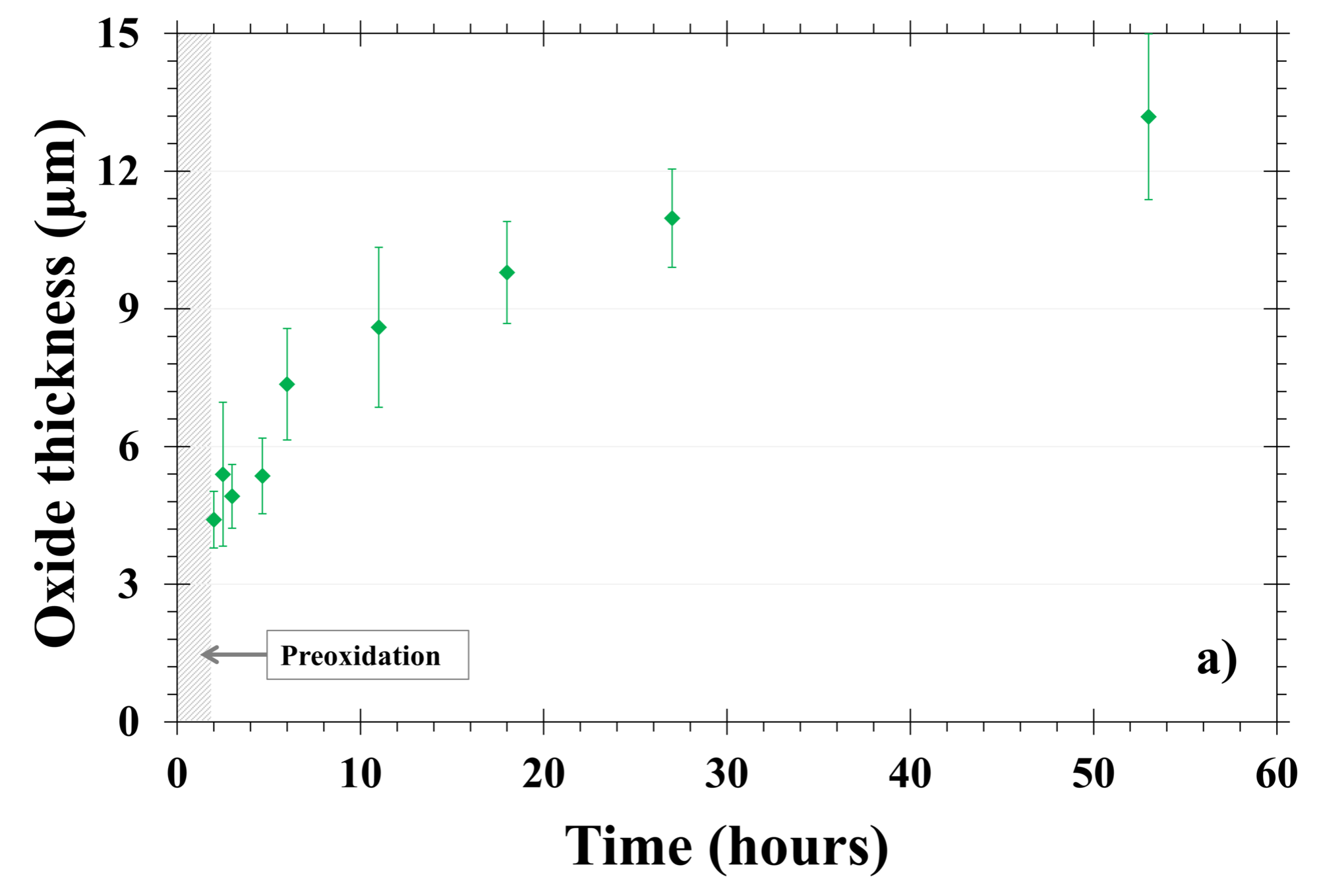
Oxide thickness (µm)
15
12
9
6
3
0
0
10
20
30
40
50
60
Time (hours)
Preoxidation
a)

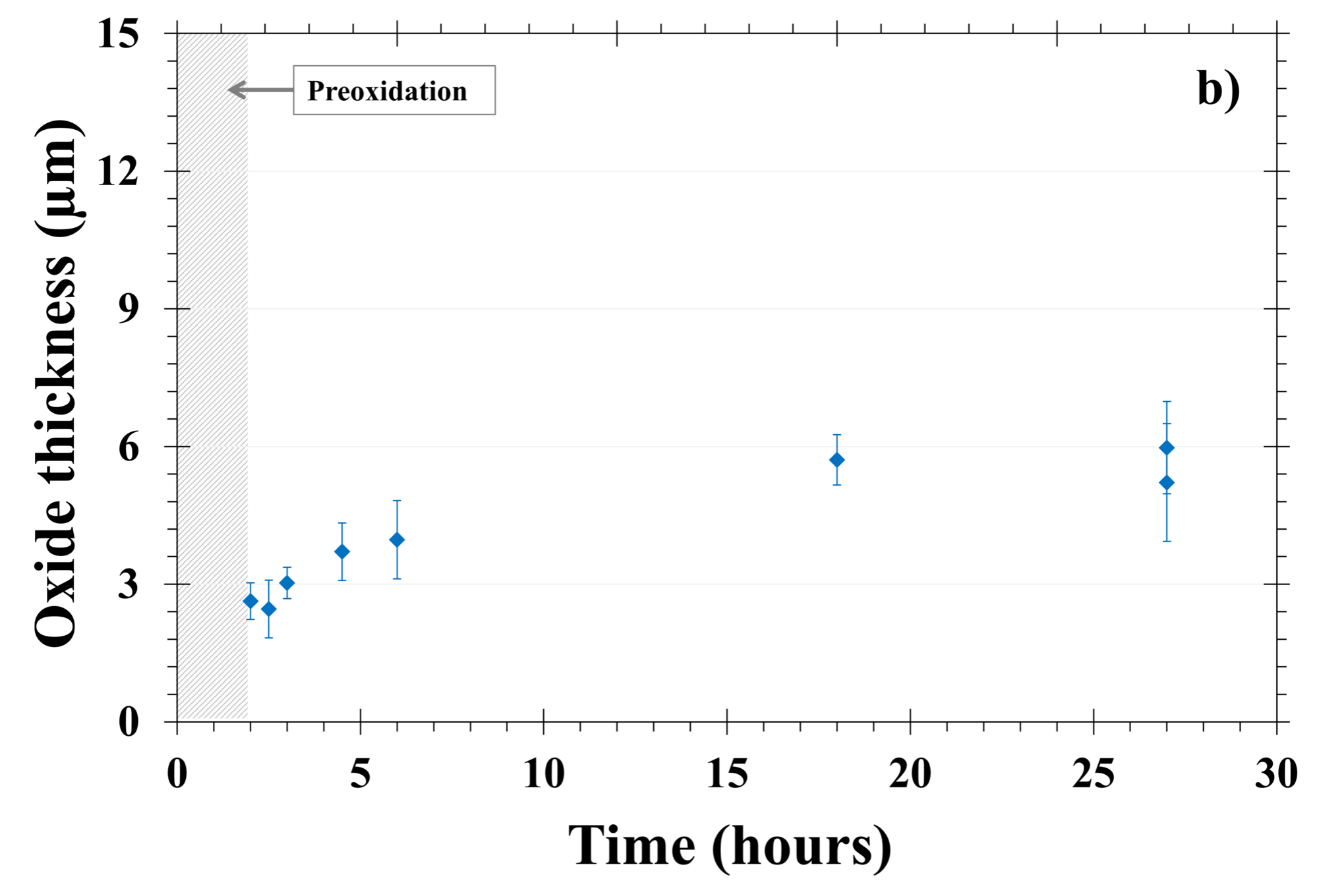
Preoxidation
b)
Oxide thickness (µm)
Time (hours)
0
3
6
9
12
15
0
5
10
15
20
25
30

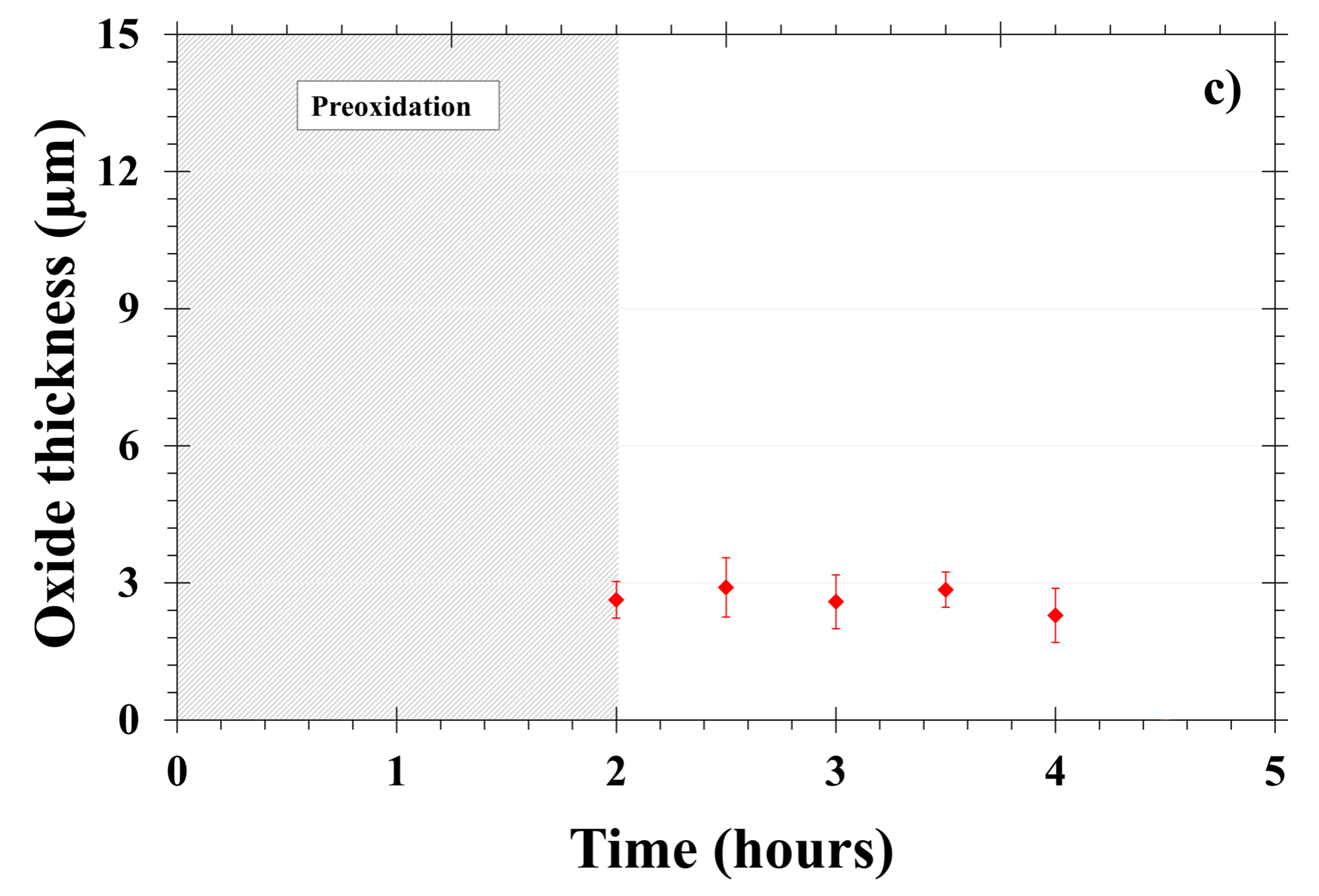
Preoxidation
c)
Oxide thickness (µm)
Time (hours)
0
3
6
9
12
15
0
1
2
3
4
5

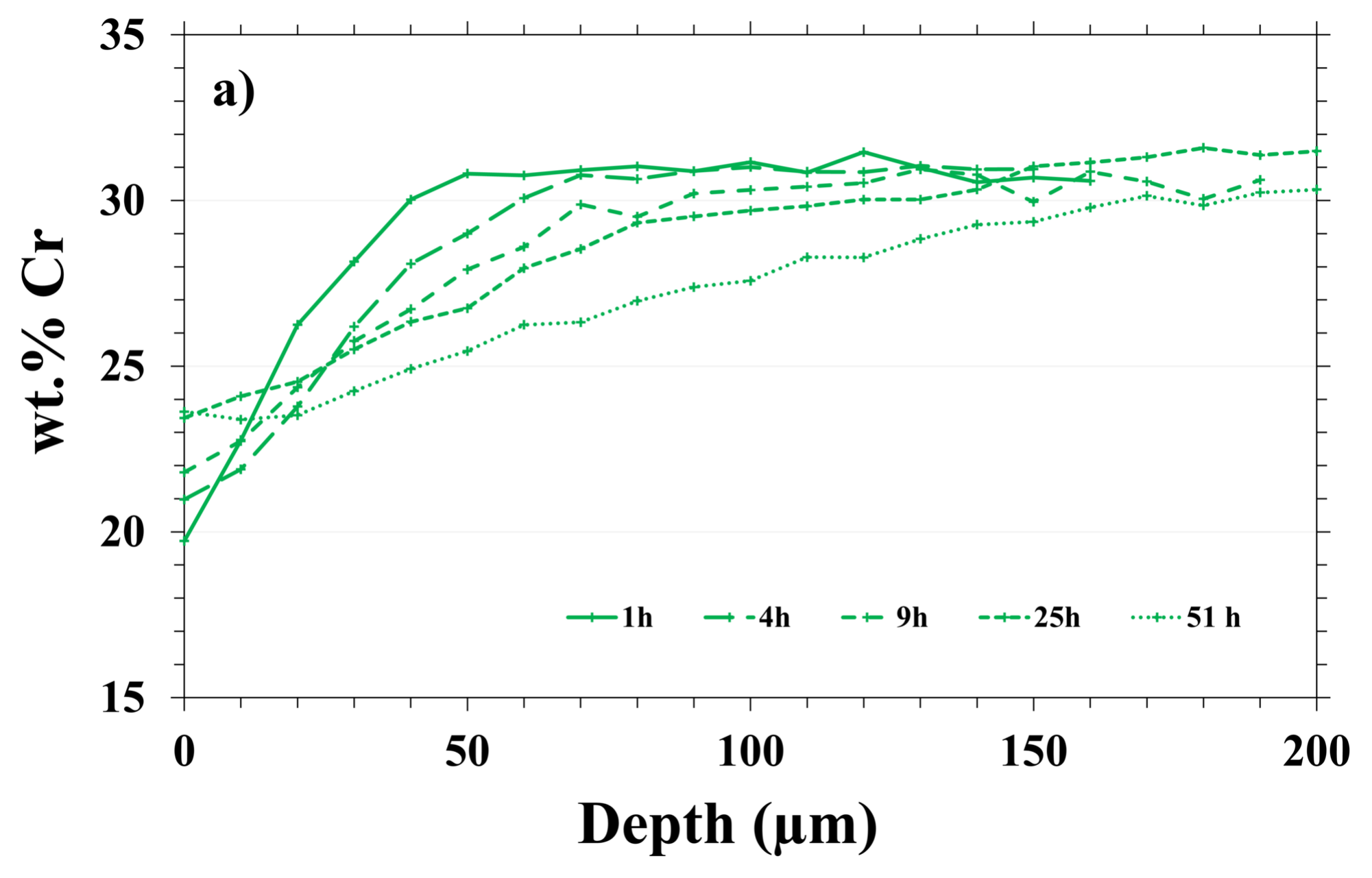
a)
wt.% Cr
35
30
25
20
15
0
50
100
150
200
Depth (µm)
1h
4h
9h
25h
51 h

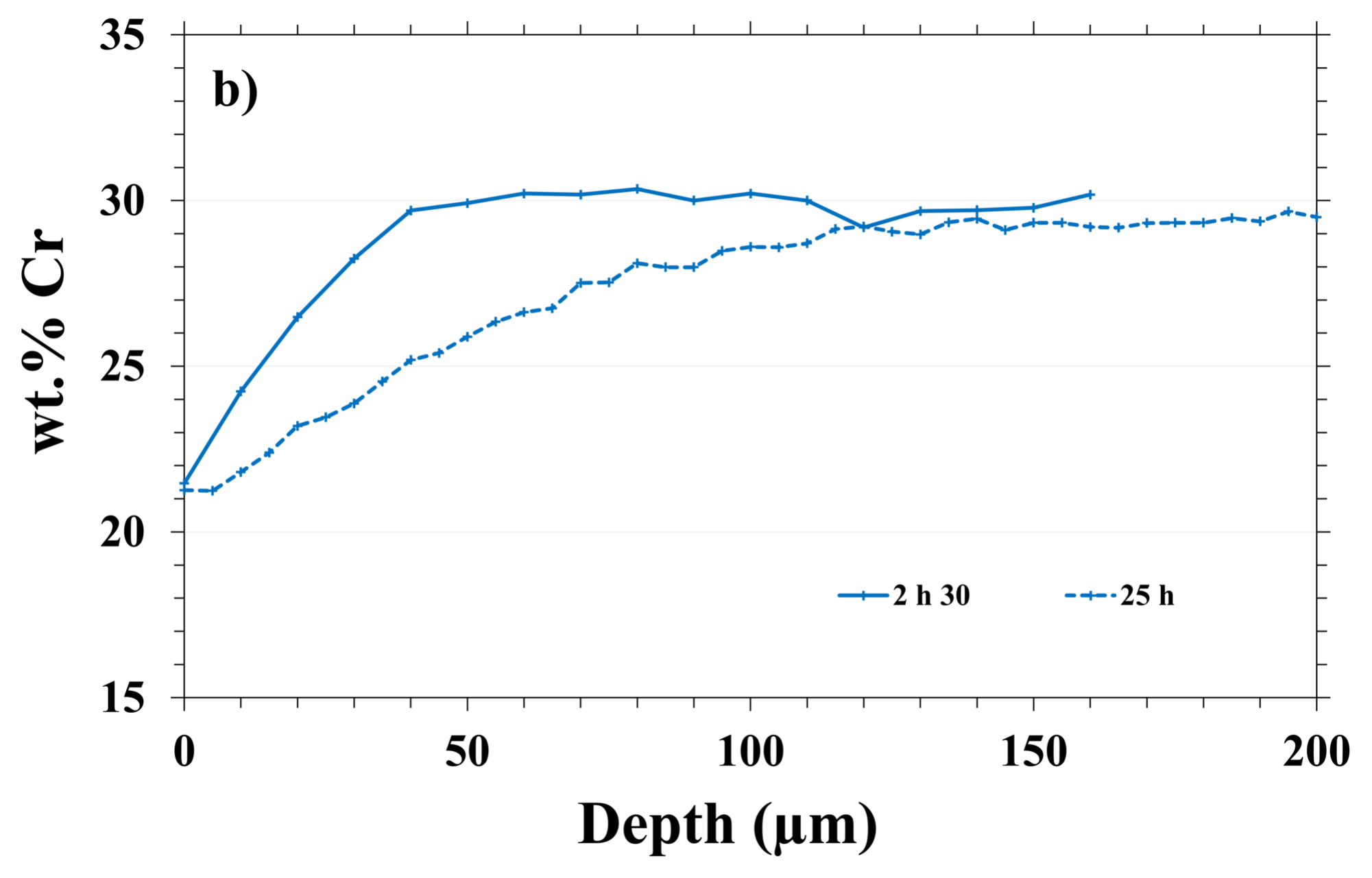
b)
wt.% Cr
35
30
25
20
15
0
50
100
150
200
Depth (µm)
2 h 30
25 h

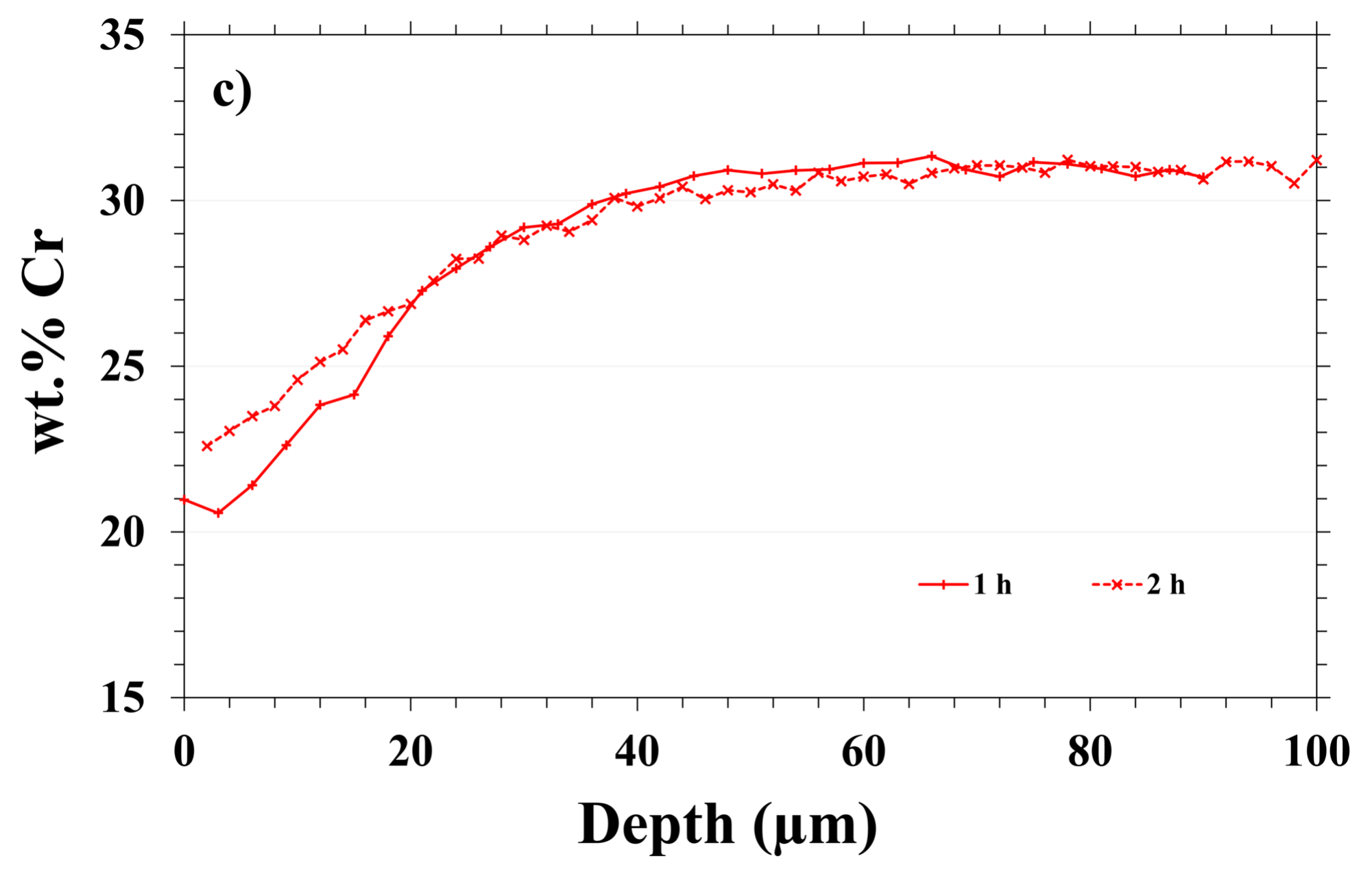
c)
wt.% Cr
35
30
25
20
15
0
20
40
60
80
100
Depth (µm)
1 h
2 h

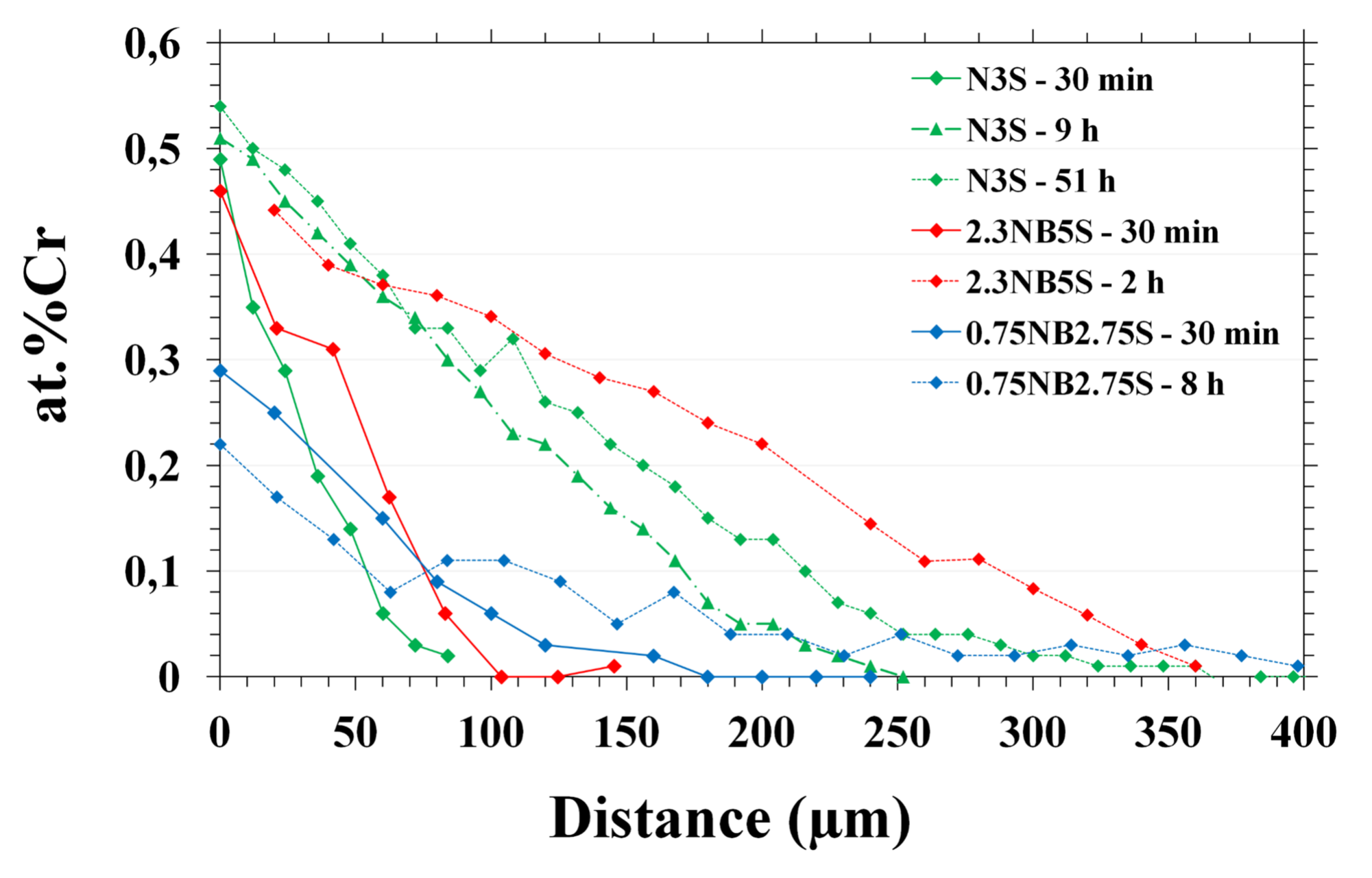
N3S - 30 min
N3S - 9 h
N3S - 51 h
2.3NB5S - 30 min
2.3NB5S - 2 h
0.75NB2.75S - 30 min
0.75NB2.75S - 8 h
at.%Cr
0,6
0,5
0,4
0,3
0,2
0,1
0
0
50
100
150
200
250
300
350
400
Distance (µm)

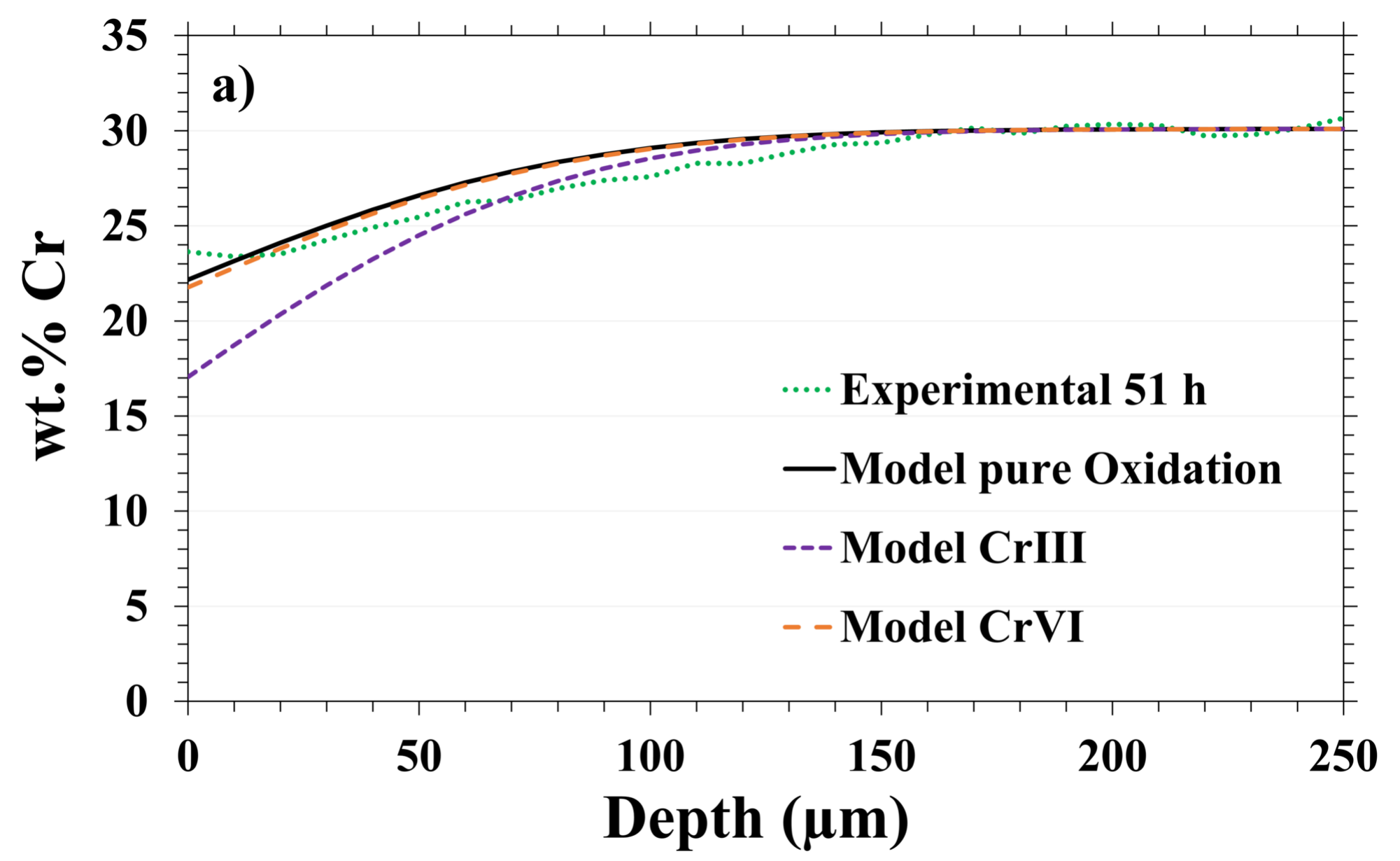
a)
wt.% Cr
Depth (µm)
0
5
10
15
20
25
30
35
0
50
100
150
200
250
Experimental 51 h
Model pure Oxidation
Model CrIII
Model CrVI

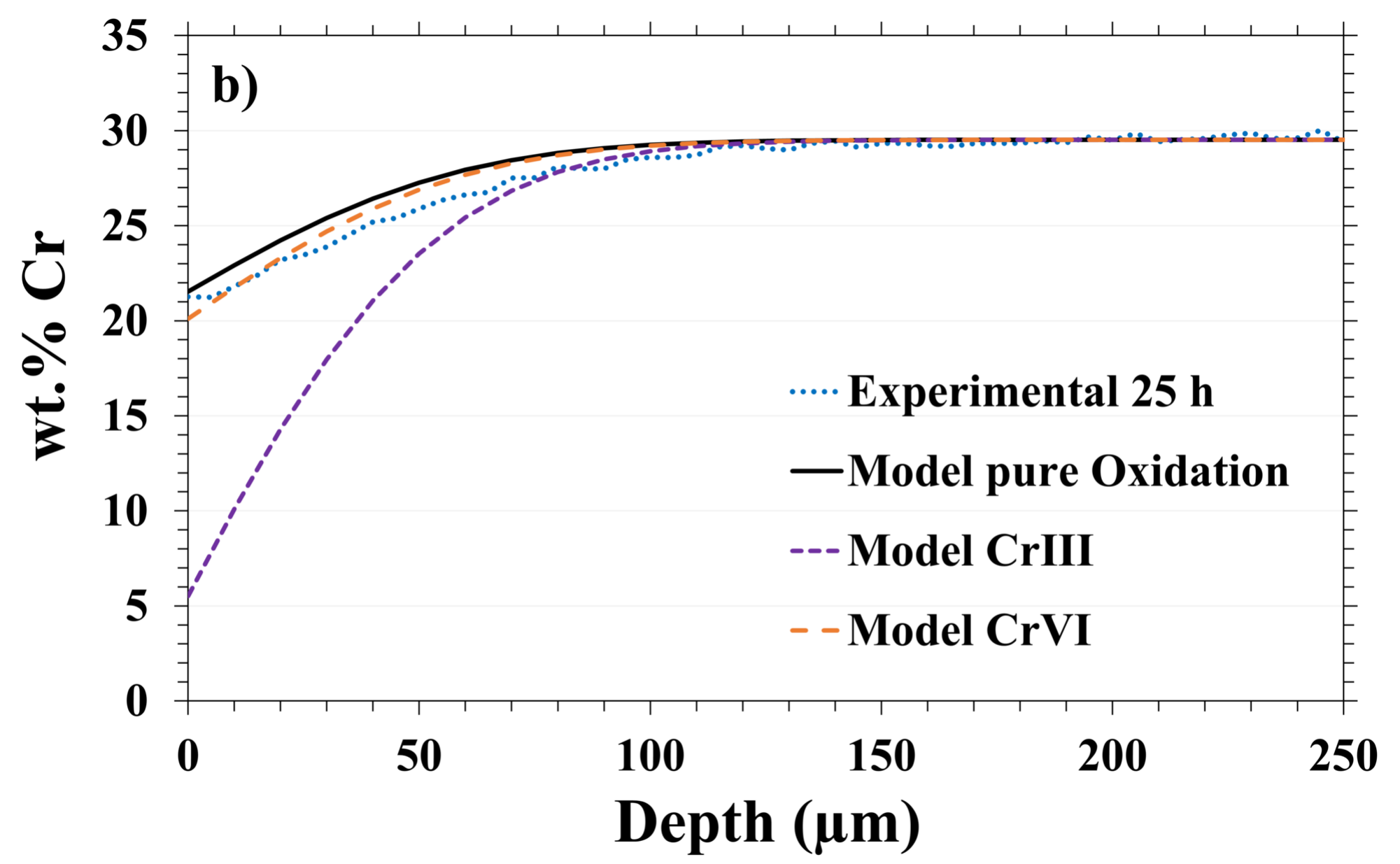
b)
wt.% Cr
Depth (µm)
0
5
10
15
20
25
30
35
0
50
100
150
200
250
Experimental 25 h
Model pure Oxidation
Model CrIII
Model CrVI

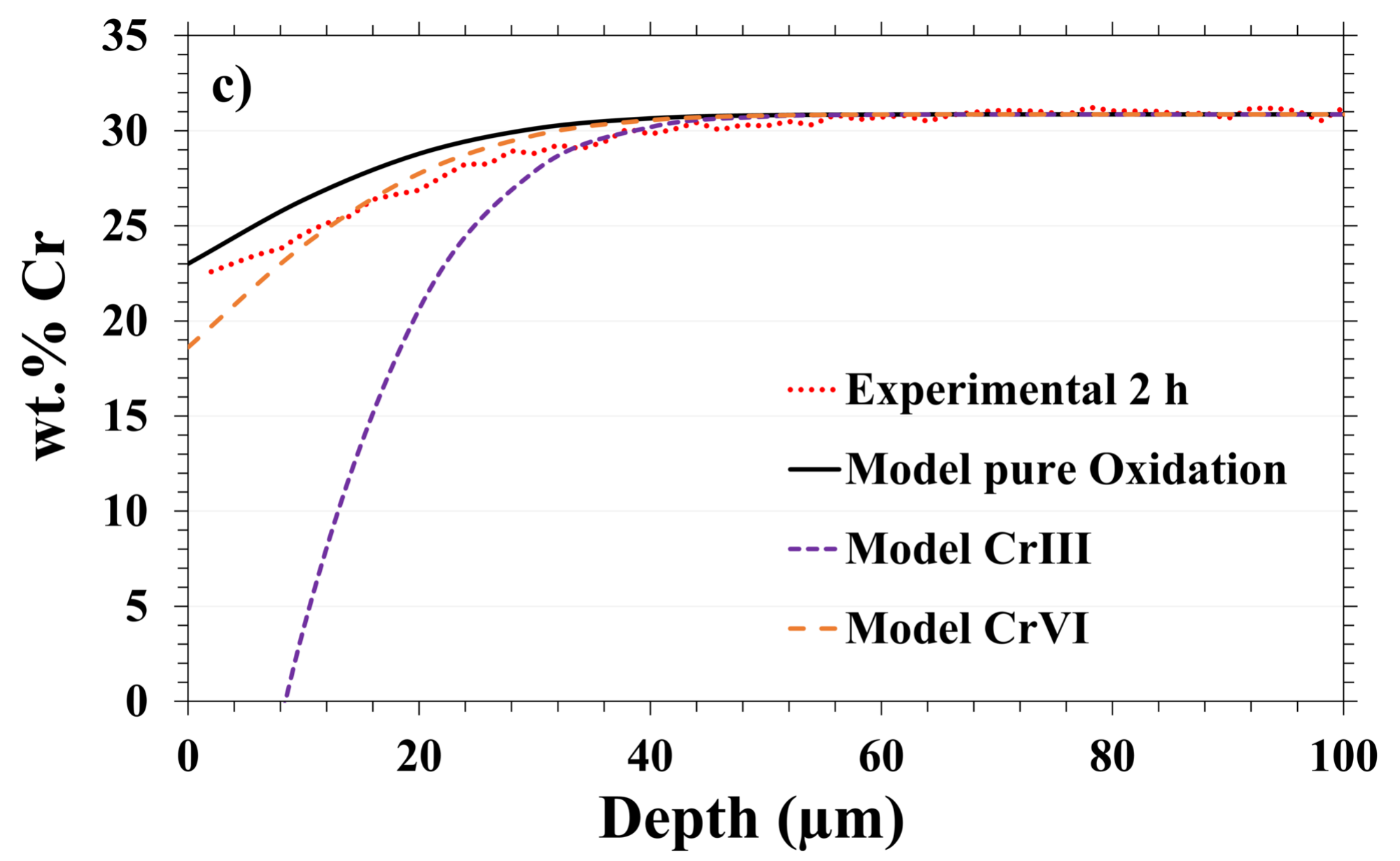
c)
wt.% Cr
Depth (µm)
0
5
10
15
20
25
30
35
0
20
40
60
80
100
Experimental 2 h
Model pure Oxidation
Model CrIII
Model CrVI

a)

Oxide thickness (µm)

Time (hours)

Preoxidation

Experimental
numerical model CrIII
numerical model CrVI
analytical model CrIII
analytical model CrVI

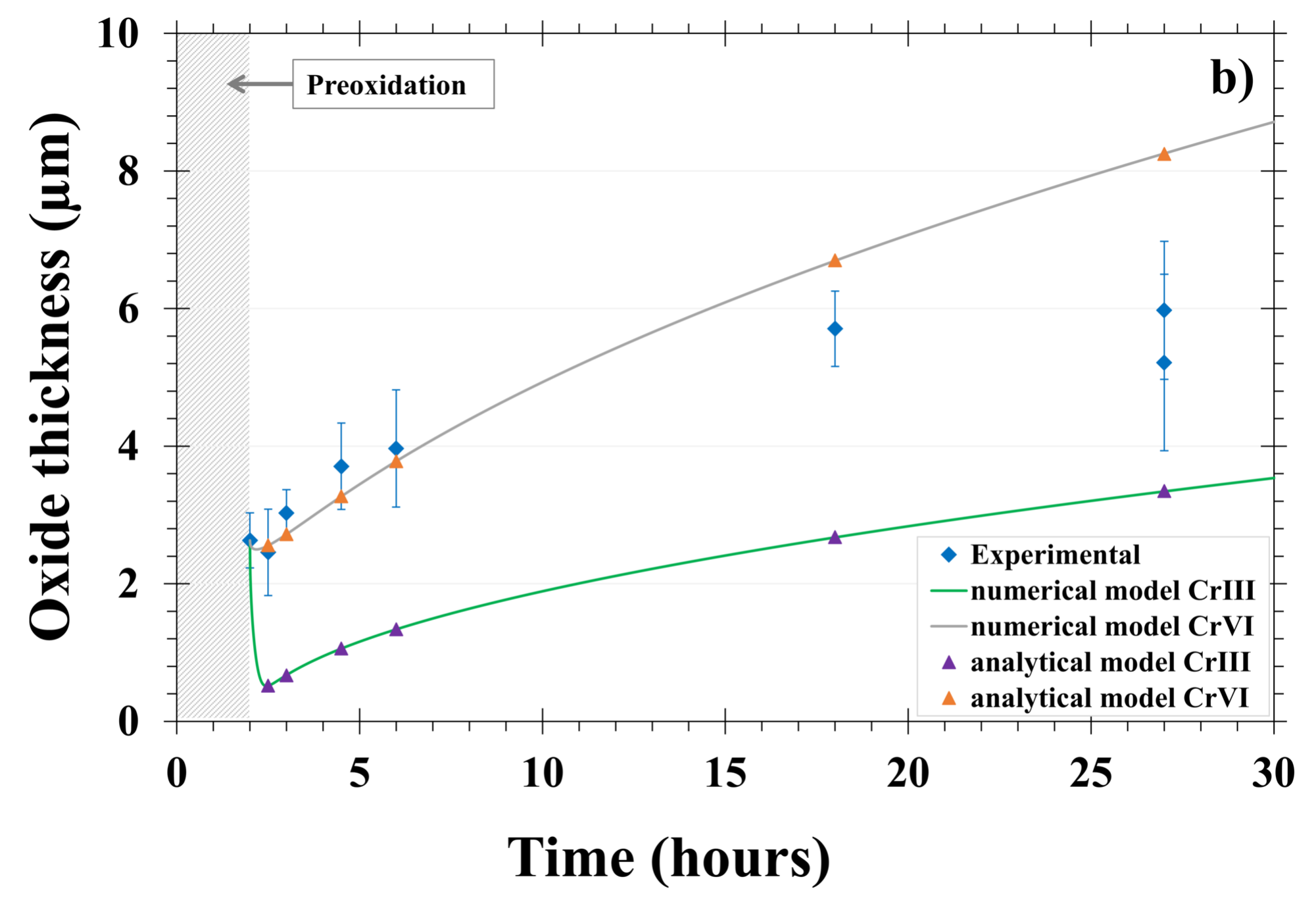
b)
Preoxidation
Oxide thickness (µm)
Time (hours)
0
2
4
6
8
10
0
5
10
15
20
25
30
Experimental
numerical model CrIII
numerical model CrVI
analytical model CrIII
analytical model CrVI

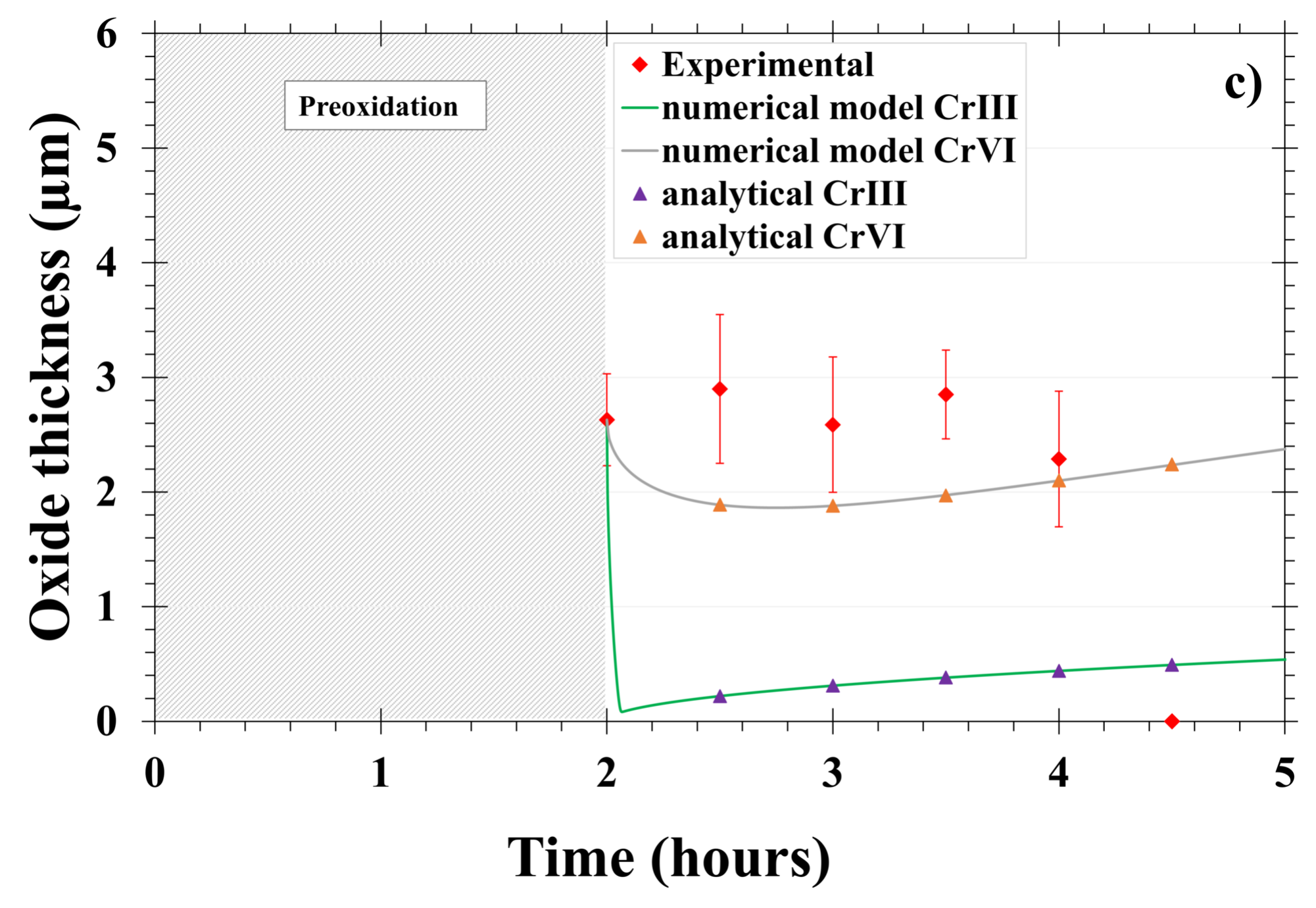
Preoxidation
Experimental
numerical model CrIII
numerical model CrVI
analytical CrIII
analytical CrVI
c)
Oxide thickness (µm)
Time (hours)
0
1
2
3
4
5
6